Supporting Information

Fluorescence behavior of 5,10-disubstituted [5]helicene derivatives in solution and the effect of self-assembly on their radiative and non-radiative rate constants

Takashi Hirose,[a] Natsuki Ito,[a] Hiromu Kubo,[a] Tohru Sato[b,c] and Kenji Matsuda*[a]

[a] *Department of Synthetic Chemistry and Biological Chemistry, Graduate School of Engineering, Kyoto University, Katsura, Nishikyo-ku, Kyoto 615-8510, Japan*

[b] *Department of Molecular Engineering, Graduate School of Engineering, Kyoto University, Katsura, Nishikyo-ku, Kyoto 615-8510, Japan*

[c] *Unit of Elements Strategy Initiative for Catalysts & Batteries, Kyoto University, Katsura, Nishikyo-ku, Kyoto 615-8510, Japan*

E-mail: kmatsuda@sbchem.kyoto-u.ac.jp

Contents:

Experimental Details

Supporting Data

References

Experimental details

A. Synthesis and Materials

1,4-Bis(2-cyano-2-(3-methoxyphenyl)ethenyl)-2,3-dimethoxybenzene (6b).

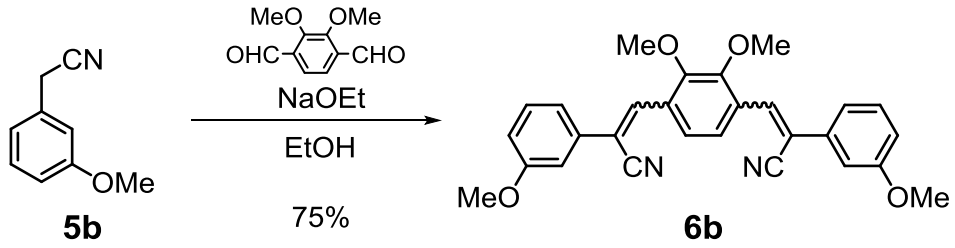

To a solution of 1,4-diformyl-2,3-dimethoxybenzene (310 mg, 1.6 mmol) and 3-methoxyphenylacetonitrile (**5b**) (520 mg, 3.5 mmol) in dry ethanol (15 mL) was added sodium ethoxide (320 mg, 4.6 mmol). The reaction mixture was stirred for 1 h at 50 °C. After cooling to room temperature, precipitates were filtered and washed with cold ethanol and water to give compound **6b** as a pale yellow powder (540 mg, 1.2 mmol, 75%, mixture of (*E*,*E*) and (*E*,*Z*) isomers).

^{1}H NMR ($CDCl_3$, 500 MHz, δ) 3.89 (6H, s), 3.92 (6H, s), 6.97 (2H, d, *J* = 8.9 Hz), 7.24 (2H, s), 7.32 (2H, d, *J* = 7.0 Hz), 7.39 (2H, t, *J* = 7.9 Hz), 7.89 (2H, s), 8.08 (2H, s); MALDI-HRMS *m*/*z* $[M]^+$ calcd for $C_{28}H_{24}N_2O_4^+$: 452.1731; found: 452.1702.

5,10-Dicyano-3,7,8,12-tetramethoxy[5]helicene. (1b)

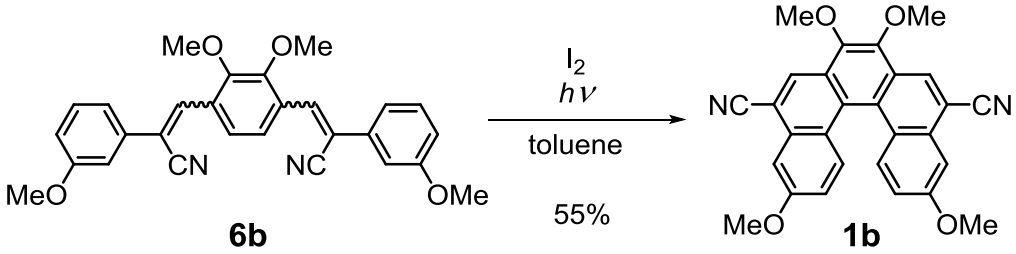

A round-bottom quartz flask was charged with compound **6b** (450 mg, 1.0 mmol), iodine (260 mg, 1.0 mmol) and toluene (25 mL). The solution was stirred and irradiated by mercury lamp (RAYONET) for 15 h. The mixture was washed with aq. $Na_2S_2O_3$ and brine, dried over $MgSO_4$, filtered, and concentrated in vacuo. The crude product was purified by silica gel column chromatography (hexane/CH_2Cl_2 = 25/75) to afford a yellow solid. To remove a structural isomer of **1b** (i.e., 5,10-dicyano-1,7,8,12-tetramethoxy[5]helicene), further purification was conducted by recrystallization from dichloromethane to give compound **1b** as a yellow crystal (250 mg, 0.55 mmol, 55%).

^{1}H NMR ($CDCl_3$, 500 MHz, δ) 4.04 (6H, s), 4.15 (6H, s), 7.02 (2H, dd, *J* = 9.2 Hz, 2.7 Hz), 7.63 (2H, d, *J* = 2.4 Hz), 8.17 (2H, d, *J* = 9.5 Hz), 8.76 (2H, s); ^{13}C NMR ($CDCl_3$, 126 MHz, δ) 55.6, 61.3, 104.2, 109.9, 118.0, 125.1, 126.0, 127.2, 128.5, 130.4, 131.3, 144.1, 159.2; MALDI-HRMS *m*/*z* $[M]^+$ calcd for $C_{28}H_{20}N_2O_4^+$, 448.1418; found, 448.1405.

3,7,8,12-tetramethoxy[5]helicene-5,10-dicarboxylic acid (4b)

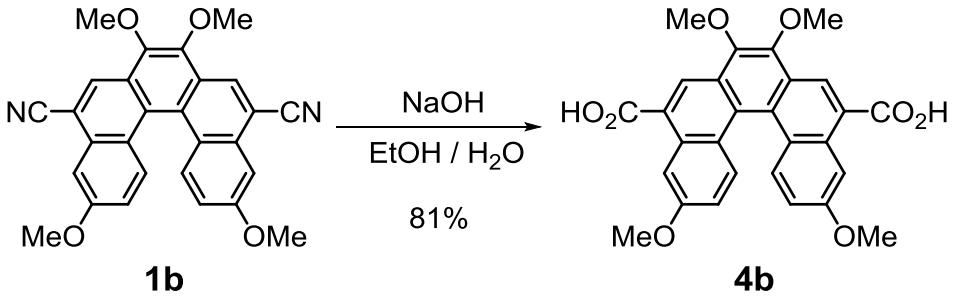

1b **4b**

To a suspension of compound **1b** (250 mg, 0.55 mmol) in ethanol (6 mL) was added aq. NaOH (10 M, 6 mL). The mixture was refluxed for 30 h. After cooling to room temperature, the resulting solution was acidified by conc. HCl. The precipitate was filtrated and washed by water to afford compound **4b** as a pale yellow powder (220 mg, 0.45 mmol, 81%).

^{1}H NMR (DMSO-d_6, 500 MHz, δ) 3.93 (6H, s), 4.12 (6H, s), 7.05 (2H, dd, J = 9.2 Hz, 2.7 Hz), 8.13 (2H, d, J = 9.5 Hz), 8.42 (2H, d, J = 2.7 Hz), 8.90 (2H, s), 13.44 (2H, s); ^{13}C NMR ($CDCl_3$, 126 MHz, δ) 55.1, 61.2, 105.7, 116.0, 124.6, 125.4, 125.6, 126.2, 127.0, 129.8, 130.4, 144.0, 157.9, 168.3; MALDI-HRMS m/z $[M]^+$ calcd for $C_{28}H_{22}O_8^+$: 486.1309; found: 486.1292.

B. UV-vis., CD, and Fluorescence Spectroscopy

Absorption spectra were measured on a JASCO V-670 spectrophotometer (conditions: scan rate, 200 nm/min; band width, 1 nm) equipped with a ETCS-761 Peltier-type temperature controller. For variable-temperature measurement, heating and cooling rate was set at 5 °C/min and the sample solution was kept for 10 minutes at a target temperature before recording a spectrum. CD spectra were measured on a JASCO J-720WI (conditions: scan rate, 100 nm/min; response, 1 sec; slit width, 1 nm). Fluorescence spectra were measured on a HORIBA SPEX Fluorolog-3 fluorescence spectrophotometer. Fluorescence quantum yields in solution were determined on a Hamamatsu Photonics Absolute quantum yield measurement system C6620-02G. Fluorescence lifetime were recorded on a Hamamatsu Photonics picosecond fluorescence lifetime measurement system C11200 equipped with picosecond light pulser PLP-10, spectrograph C11119-01, and streakscope C10627. Excitation was carried out by a laser diode, whose wavelength was λ = 378 nm and pulse width was around 45 ps. Fluorescence emission rate constants (k_f) and nonradiative decay rate constants (k_{nr}) were calculated from the fluorescence quantum yield (Φ_f) and the area-weighted mean fluorescence lifetime ($<\tau_f>$) by using the following equations,

$$\Phi_f = \frac{k_f}{k_f + k_{nr}} = k_f \langle \tau_f \rangle \quad \text{(S1)}$$

$$\langle \tau_f \rangle = \frac{1}{k_f + k_{nr}} \quad \text{(S2)}$$

For the spectroscopic measurements, a quartz cuvette with 10 mm optical path was used for the sample of compound **2a** (typically, $c = 1 \times 10^{-5}$ M), and that with 1 mm optical path was used for the sample of compound **3a** and **3b** (typically, $c = 1 \times 10^{-4}$ M) to avoid distortion of spectrum due to the effect of self-absorption.

C. TEM measurements

TEM microscopy was conducted on a JEOL JEM-1400 instrument. The acceleration voltage was set at 100 kV. For the sample of compound **2a**, an aqueous solution in water/MeCN (99/1, v/v, $c = 1 \times 10^{-4}$ M, 2 μL) was dropped on a carbon-coated copper grid and dried at room temperature. After being completely dried, the copper grid was exposed to OsO_4 vapor using a Filigen VSC1R1 Vacuum Stain Equipment (pressure of OsO_4 vapor, 500 Pa; stain time, 10 minutes; at room temperature). For the sample of compounds **3a** and **3b**, a heptane solution ($c = 1 \times 10^{-4}$ M, 5 μL) was dropped on a carbon-coated copper grid and dried at room temperature. This drop-and-dry process was repeated for 5 times. After being completely dried, the sample was subjected to TEM measurement without any staining treatment.

D. DLS measurements

Size distribution of aggregates composed of compound **2a** was measured on a DLS instrument Nicomp 380ZLS particle sizer equipped with a 785 nm red laser as a light source and a peltier-type , using a fixed angle (90°) at room temperature. An appropriate channel width was automatically determined depending on the decay time of observed autocorrelation functions. The Nicomp algorithm was adopted to analyze size distribution from the observed autocorrelation functions.

E. Theoretical calculations

The geometrical optimization was carried out at the RB3LYP/6-31g(d) level of theory implemented on Gaussian 09 package.[S1] Convergence at a local minimum structure was confirmed by no imaginary frequencies on frequency analysis. Successively the optimized local minimum structures were subjected to time-dependent (TD) DFT calculations to obtain excited states at the same level of theory. Six octyl groups of compounds **3a** and **3b** were replaced by methyl group in order to simplify calculations. Details of vibronic coupling constant (VCC) and vibronic coupling density (VCD) analyses are described in elsewhere.[S2,S3]

Supporting Data

Temperature dependent absorption spectra

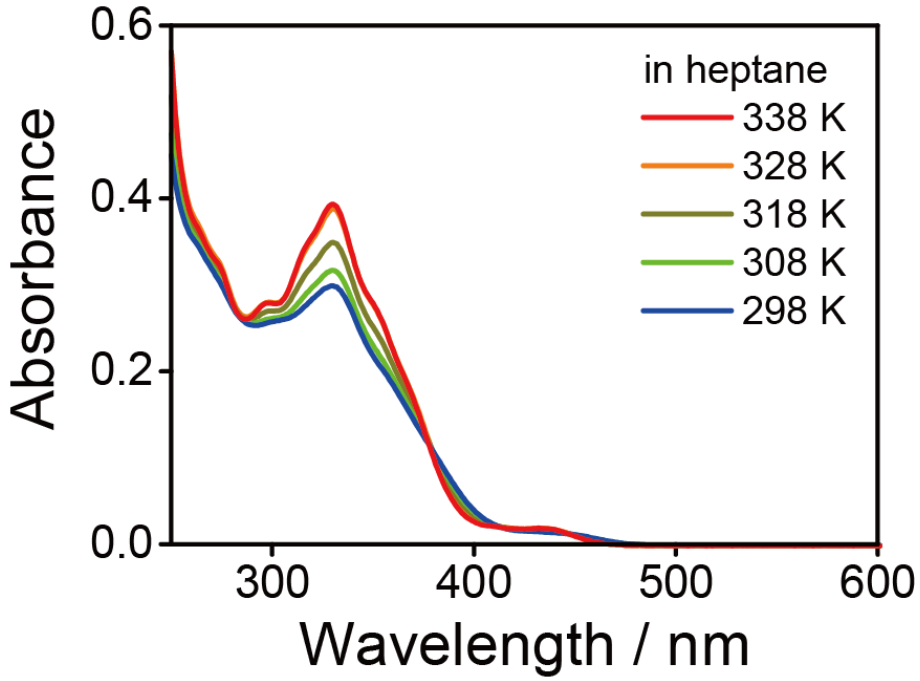

Figure S1. Temperature-dependent absorption spectra of compound **3b** in hexane (c = 1 × 10^{-4} M). Corresponding spectra of compound **3a** is shown in Fig. 3d in the main text.

Isolation of enantiomer of compound 2a by a chiral HPLC

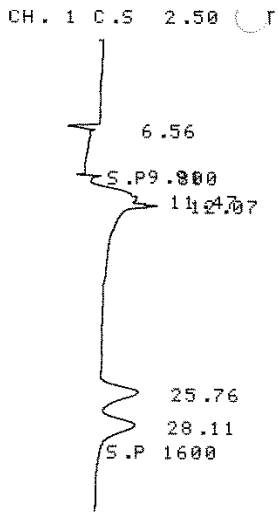

D-2500 07/10/14 16:45

METHOD: TAG: 4 CH: 1

FILE: 0 CALC-METHOD: AREA% TABLE: 0 CONC: AREA

NO.	RT	AREA	CONC	BC
1	6.56	17129	12.142	BB
2	9.91	3843	2.724	BV
3	11.47	30451	21.586	VV
4	12.07	39452	27.967	VB
5	25.76	23044	16.336	BV
6	28.11	27148	19.245	VB
TOTAL		141067	100.000	

PEAK REJ : 0

P.168

Figure S2. (a) Chiral HPLC chart for the racemic **2a**. Conditions: HPLC column, CHIRALPAC IC 250–4.6 mm (5 μm); eluent, methanol; flow rate, 0.5 mL/min; detection wavelength, 260 nm; R_f = 25.8 and 28.1 min for (−)-**2a** and (+)-**2a**, respectively.

Isolation of enantiomer of compound 3a by a chiral HPLC

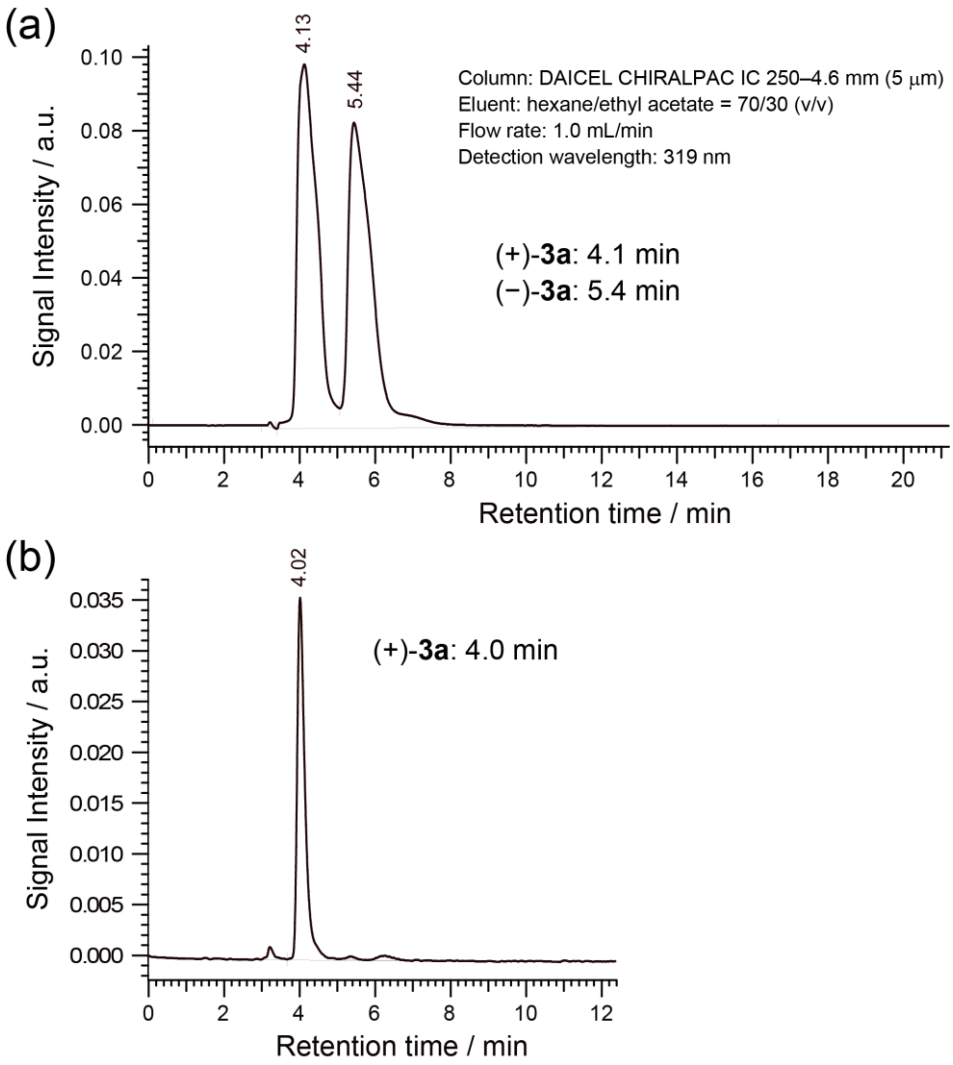

Figure S3. (a) Chiral HPLC chart for the racemic **3a**. Conditions: HPLC column, CHIRALPAC IC 250–4.6 mm (5 μm); eluent, hexane/ethyl acetate (70/30, v/v); flow rate, 1.0 mL/min; detection wavelength, 319 nm; R_f = 4.1 and 5.4 min for (+)-**3a** and (−)-**3a**, respectively. (b) The chart for the first fraction, (+)-**3a**, after chiral separation, whose CD spectrum is shown in Fig. S4.

Calculated and experimental UV-vis and CD spectra

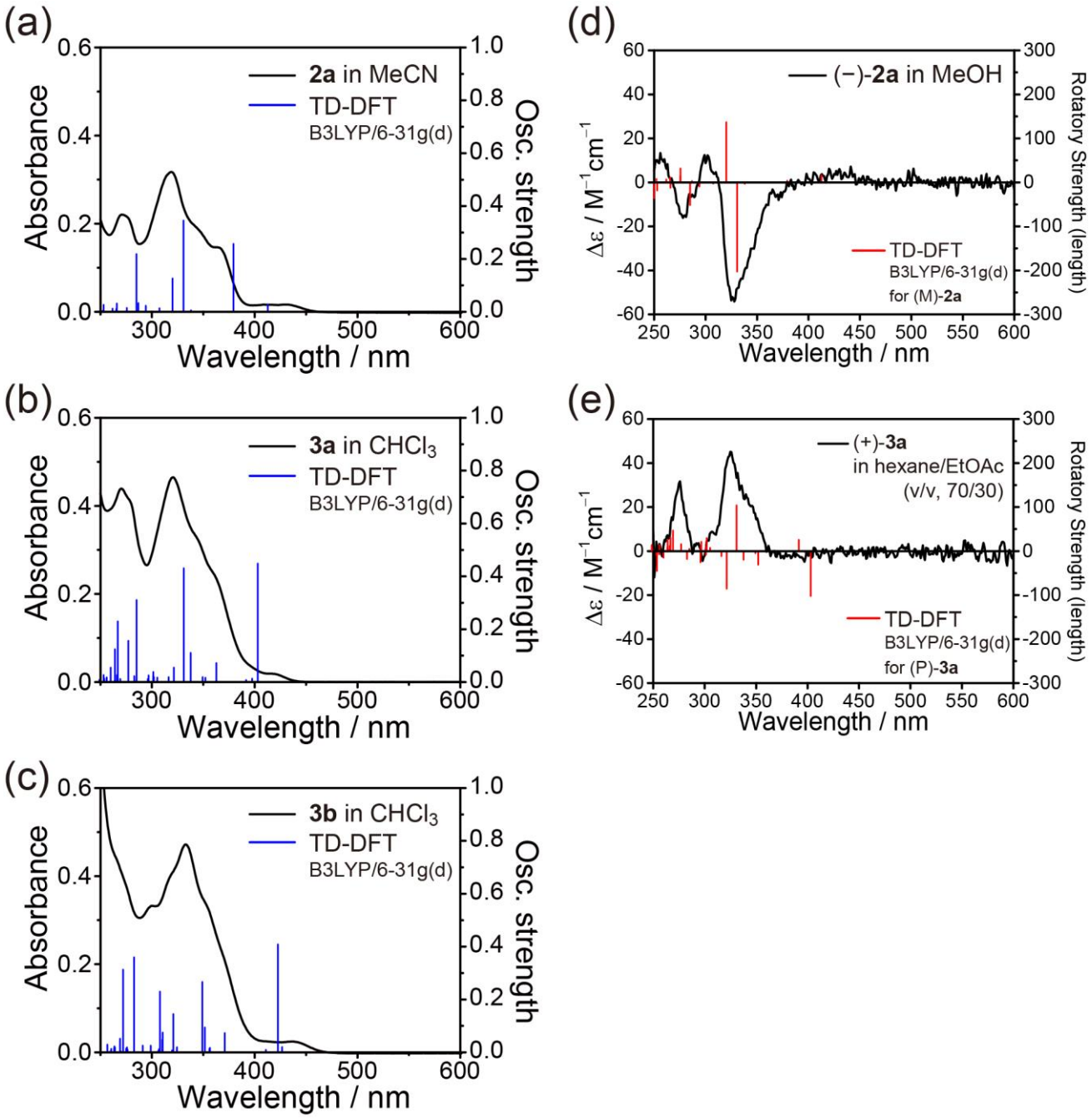

Figure S4. Calculated (blue line, at TD-B3LYP/6-31g(d) level, calced in the gas phase) and experimental UV-vis absorption spectra (black line) of (a) compound **2a** in MeCN, (b) **3a** in $CHCl_3$, and (c) **3b** in $CHCl_3$. Calculated (red line, at TD-B3LYP/6-31g(d) level, calced in the gas phase) and experimental CD spectra of (d) compound (−)-**2a** in MeOH and (e) (+)-**3a** in hexane/EtOAc (v/v, 70/30). Based on the comparison of experimental CD spectra with theoretically calculated rotatory strength, helicity of compounds **2a** and **3a** was determined as (M)-(−)-**2a** and (P)-(+)-**3a**, respectively.

Circular dichroism and rate of helical inversion

Enantiomers of compounds **2a** and **3a** were separated from racemic solution by a chiral HPLC (Figures S2 and S3) and then CD spectra were measured. To avoid any change in enantiomeric excess during removal of solvent, the sample in used eluent was directly used for CD measurement immediately after the chiral separation. For compound **2a**, the first fraction in the chiral HPLC was (−)-**2a**, which exhibits two negative cotton effects at 326 nm ($\Delta\varepsilon = -53$ $M^{-1}\cdot cm^{-1}$) and 279 nm ($\Delta\varepsilon = -16$ $M^{-1}\cdot cm^{-1}$) in methanol (Figure S5a). On the other hand, for compound **3a**, the first fraction was (+)-**3a** and two positive cotton effects were observed at 325 nm ($\Delta\varepsilon = 44$ $M^{-1}\cdot cm^{-1}$) and 275 nm ($\Delta\varepsilon = -30$ $M^{-1}\cdot cm^{-1}$) in mixed solvent of hexane/ethyl acetate (v/v, 70/30) (Figure S5b). The magnitude of CD signal of compounds **2a** and **3a** is roughly one third of parent non-substituted [5]helicene ($\Delta\varepsilon$ = 154 $M^{-1}\cdot cm^{-1}$ at 308 nm).[S4] Based on the comparison of experimental CD spectra with theoretically calculated rotatory strength, helicity of compounds (−)-**2a** and (+)-**3a** was determined as (M)-(−)-**2a** and (P)-(+)-**3a**, respectively (Figure S4).[S5]

In order to investigate the rate of helical inversion of compounds **2a** and **3a**, time-dependent change of CD signal intensity was monitored at 298 K in solution (Figures S5c and d). The decay curve could be fitted well by a mono-exponential function and the rate constant of racemization was determined. The observed half-life of racemization ($\tau_{1/2,rac}$) at 298 K was 8.5 and 10.3 hours for compounds **2a** and **3a**, respectively. The resulting half-life of racemization is slightly shorter than that of parent non-substituted [5]helicene ($\tau_{1/2,rac}$ = 15 hours at 298 K and 41 min at 323 K).[S6] Such moderate time scale of racemization of [5]helicenes is advantageous to design a dynamic system utilizing helical inversion, for example, chiroptical property associated with supramolecular system can be switched by external stimuli such as addition of a chiral source.

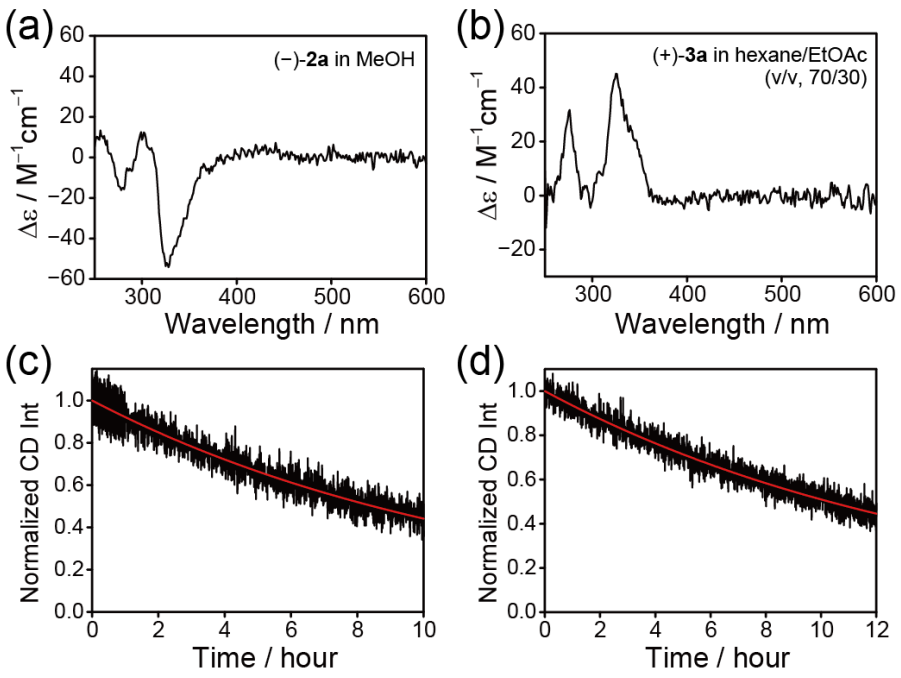

Figure S5. CD spectra of (a) (−)-**2a** in methanol ($c = 5 \times 10^{-6}$ M; at 298 K) and (b) (+)-**3a** in hexane/EtOAc (v/v, 70/30; $c = 5 \times 10^{-6}$ M; at 298 K) just after chiral separation by a chiral HPLC. Time-dependent decrease of CD intensity of (c) (−)-**2a** in methanol (at 326 nm) and (d) (+)-**3a** in hexane/EtOAc (v/v, 70/30; at 325 nm) at 298 K. Red line denotes the curves of best fit by an exponential function, from which the rate constant of racemization of **2a** and **3a** at 298 K is determined as $k_{rac} = 2.3 \times 10^{-5}$ s^{-1} and 1.9×10^{-5} s^{-1}, respectively.

TEM images of aggregates composed of compound 2a

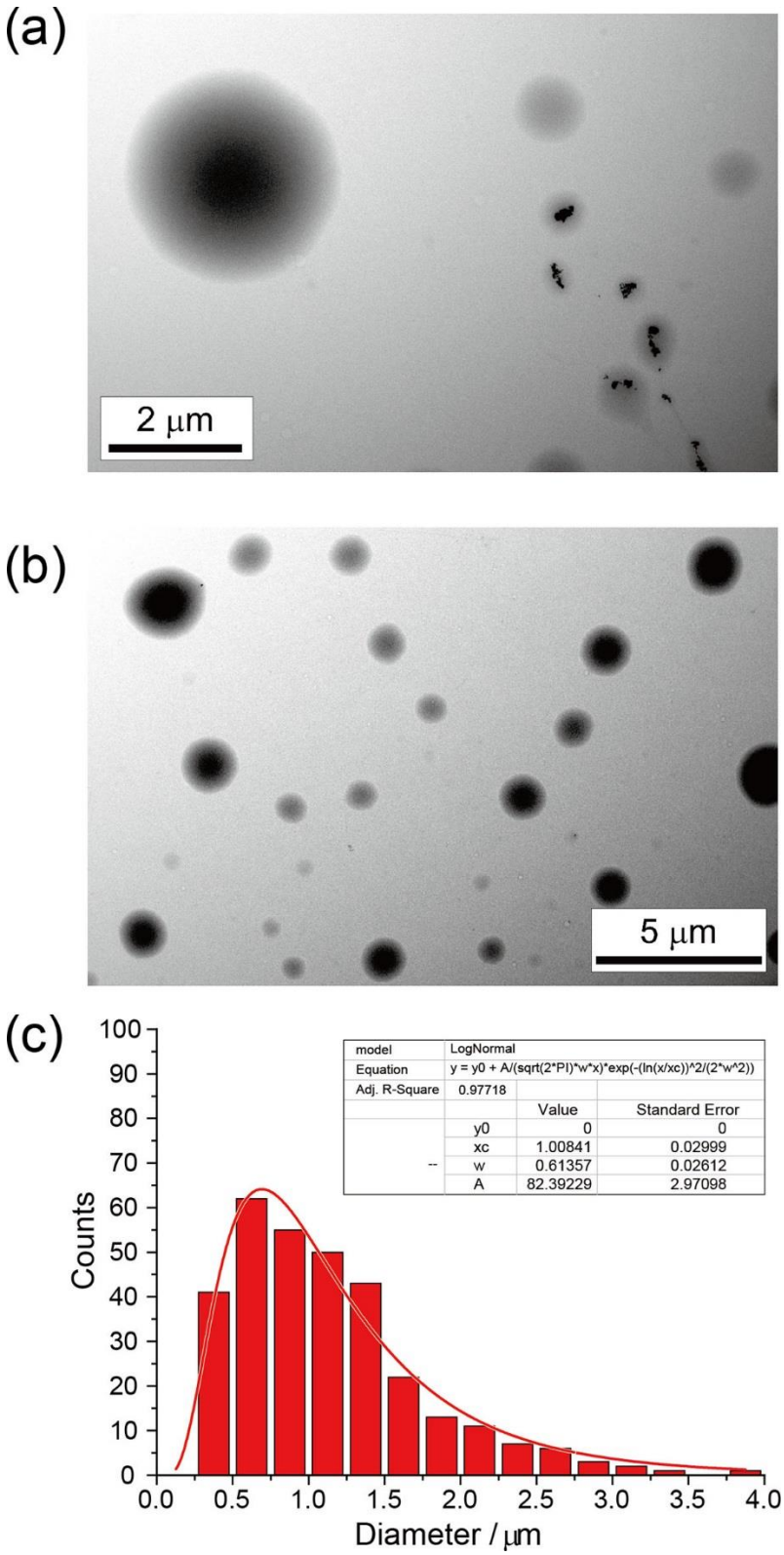

Figure S6. (a) TEM images of aggregates of compound **2a** without staining (×5.0k) and (b) after staining with OsO4 vapor (×1.5k). High contrast images of spherical aggregates composed of **2a** could be obtained by staining treatment. (c) Histogram of the diameter of the spherical aggregates (*d*) observed by totally 317 spheres by TEM images. Red line denotes the best-fitting curve by a log-normal distribution (d = 1.0 ± 0.6 μm).

Dynamic light scattering (DLS) measurement for an aqueous solution of compound 2a

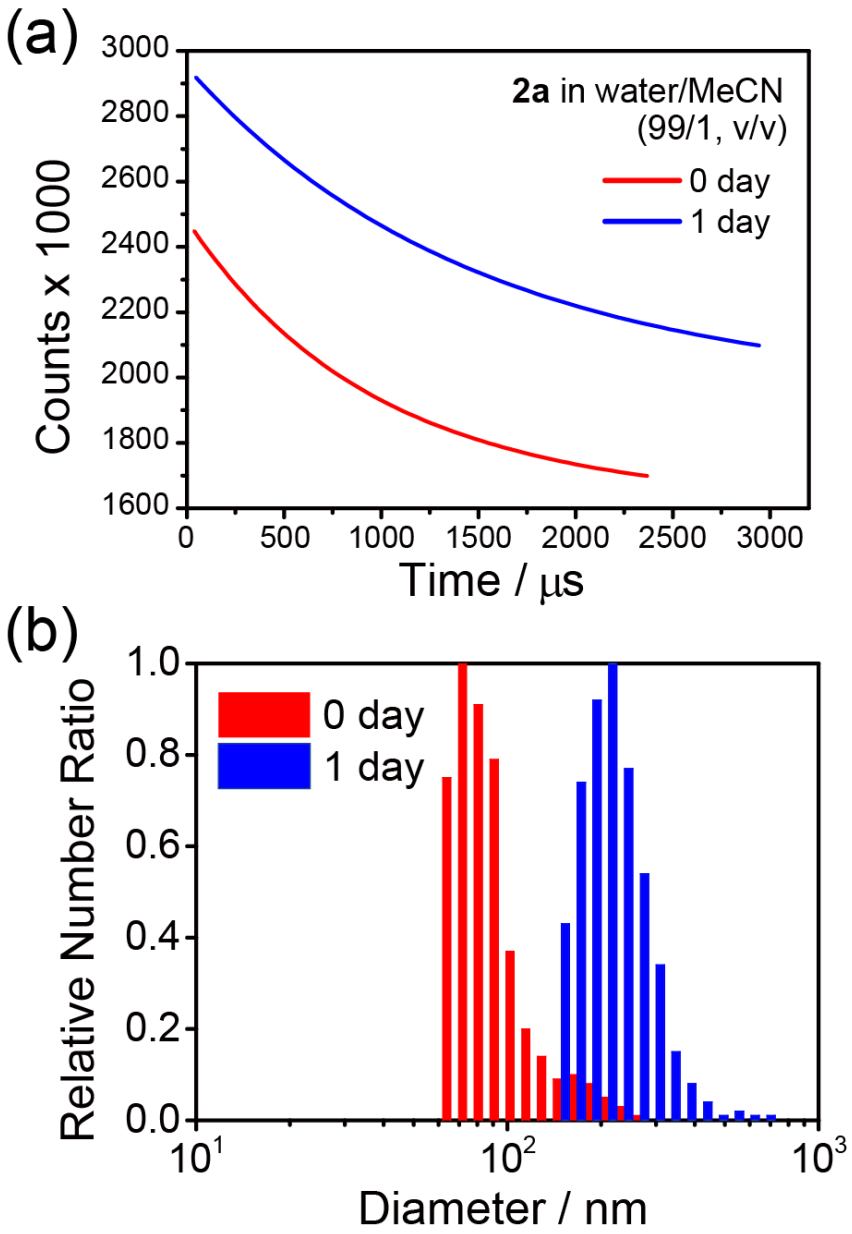

Figure S7. (a) Autocorrelation function of compound **2a** in aqueous solution (water/MeCN = 99/1, v/v; $c = 1 \times 10^{-5}$ M) observed by DLS measurement. Red line denotes the curve observed just after sample preparation (channel width = 37 μsec). Blue line denotes that of the sample after 1 day (channel width = 46 μsec). (b) Number-weighted size distribution of compound **2a**. Red bar denotes the distribution just after sample preparation ($d = 80 \pm 20$ nm) and blue bar denotes that after 1 day from sample preparation ($d = 210 \pm 50$ nm).

TEM images of aggregates composed of compound 3a

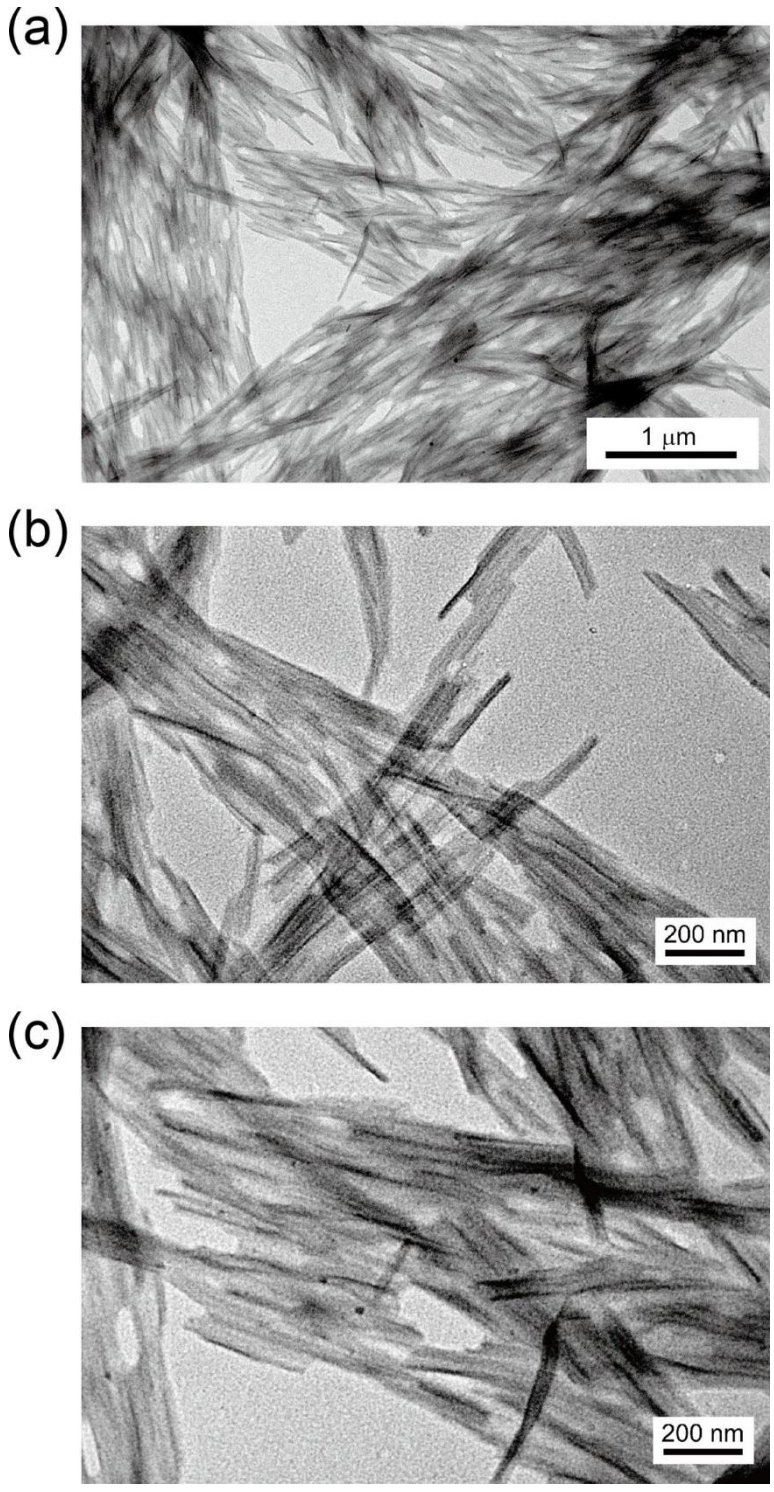

Figure S8. TEM images of aggregates of compound **3a** without staining (a, ×10k; b and c, ×30k).

TEM images of aggregates composed of compound 3b

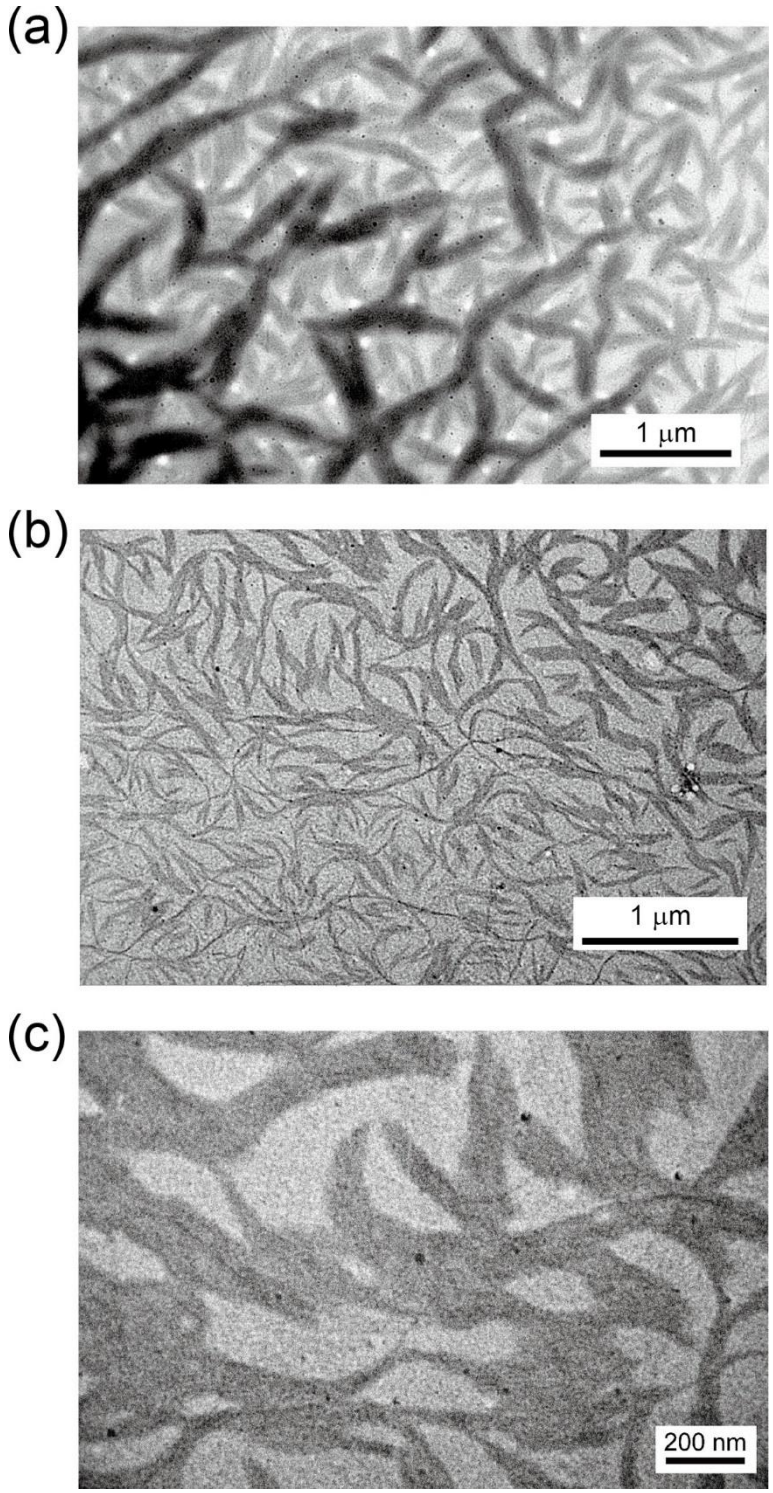

Figure S9. TEM images of aggregates of compound **3b** without staining (a, ×10k; b, ×12k; c, ×30k).

The change of fluorescence color upon aggregation on the CIE 1931 diagram

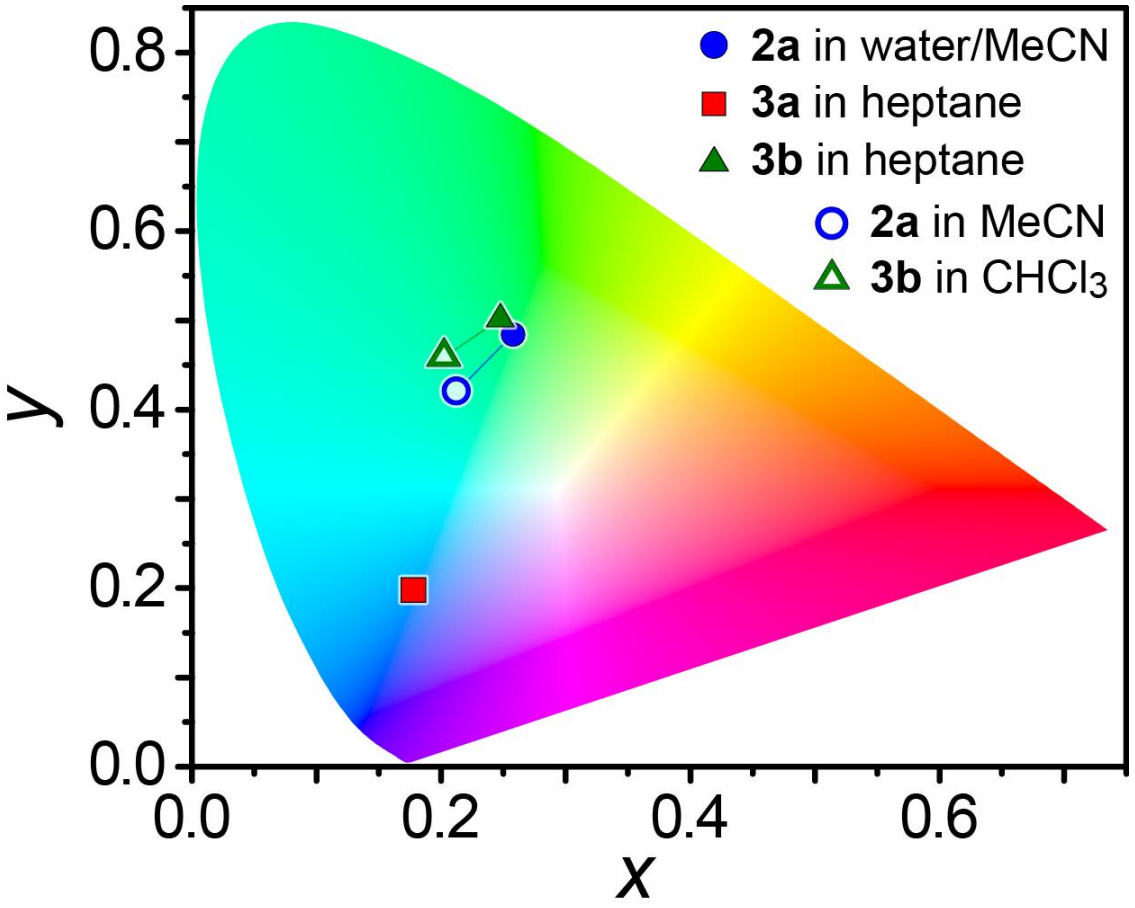

Figure S10. Emission color coordinates of compounds **2a** (blue circle), **3a** (red square), and **3b** (green triangle) in the CIE 1931 chromaticity diagram. Open and closed symbol denote the coordinates of monomer state and aggregates, respectively. Compound **3a** is non-fluorescent in the monomer state. The color change upon aggregation is moderate for compounds **2a** and **3b**.

Table S1. Fluorescence lifetime of compounds 1–3 in solution phase at room temperature [a]

compound	solvent	τ_1 (ns)	τ_2 (ns)	τ_3 (ns)	$<\tau_f>$ (ns)	χ^2
1a	$CHCl_3$	4.41 (30%)	9.16 (70%)	–	7.7	1.12
2a	MeCN	7.10 (83%)	23.8 (17%)	–	9.9	1.09
2a	water	5.30 (76%)	32.8 (24%)	–	12.0	1.18
3a	$CHCl_3$	– [d]	– [d]	– [d]	– [d]	– [d]
3a	MCH	0.32 (65%)	1.89 (23%)	9.08 (11%)	1.7	1.46
3a	heptane	3.28 (55%)	10.9 (45%)	–	6.7	1.29
3b	$CHCl_3$	0.85 (96%)	5.45 (4%)	–	1.0	1.68
3b	MCH	1.65 (55%)	3.75 (45%)	–	2.6	1.12
3b	heptane	3.23 (62%)	6.56 (38%)	–	4.5	1.74

[a]Fluorescence lifetimes were recorded upon excitation at 378 nm. [b]The area-weighted ratio ($A_n \cdot \tau_n$) are shown in parentheses. [c]The area-weighted mean fluorescence lifetime $<\tau_f>$ was calculated as follows: $<\tau_f> = \Sigma(A_n \cdot \tau_n^2)/\Sigma(A_n \cdot \tau_n)$ where A_n is the coefficients of the *n*-th component. [d]Emission was not detected.

Time-resolved fluorescence spectra using a streak scope

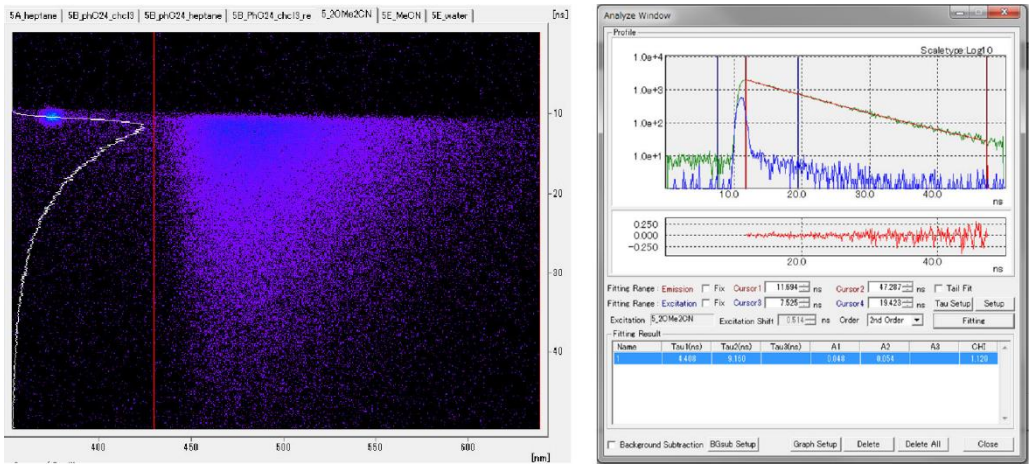

Figure S11. Streak image (left) and fluorescence decay analysis (right) of compound **1a** in $CHCl_3$.

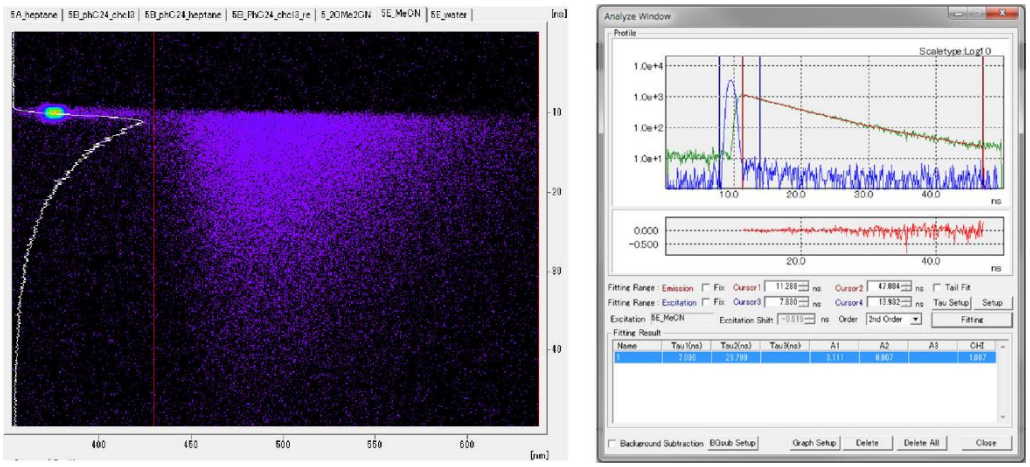

Figure S12. Streak image (left) and fluorescence decay analysis (right) of compound **2a** in MeCN ($c = 1.0 \times 10^{-5}$ M).

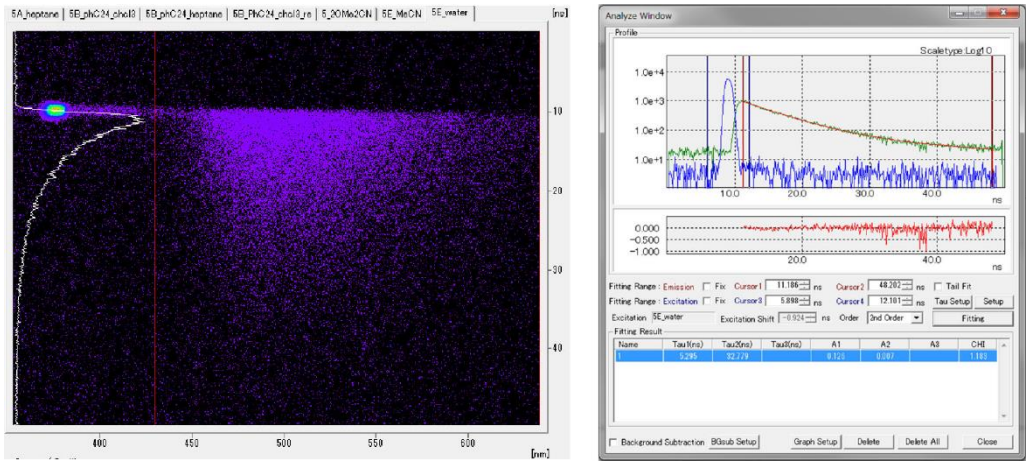

Figure S13. Streak image (left) and fluorescence decay analysis (right) of compound **2a** in aqueous media (water/MeCN = 99/1, v/v; $c = 1.0 \times 10^{-5}$ M).

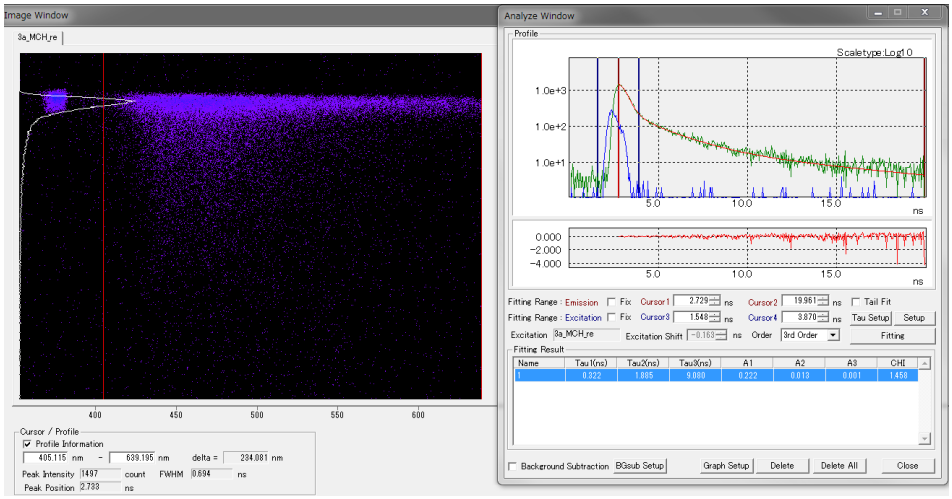

Figure S14. Streak image (left) and fluorescence decay analysis (right) of compound **3a** in MCH ($c = 1 \times 10^{-4}$ M).

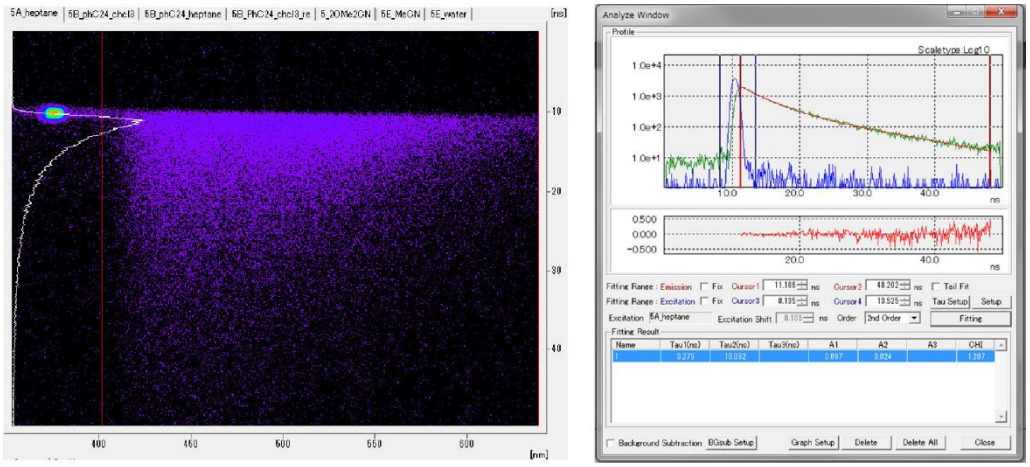

Figure S15. Streak image (left) and fluorescence decay analysis (right) of compound **3a** in heptane ($c = 1.0 \times 10^{-4}$ M).

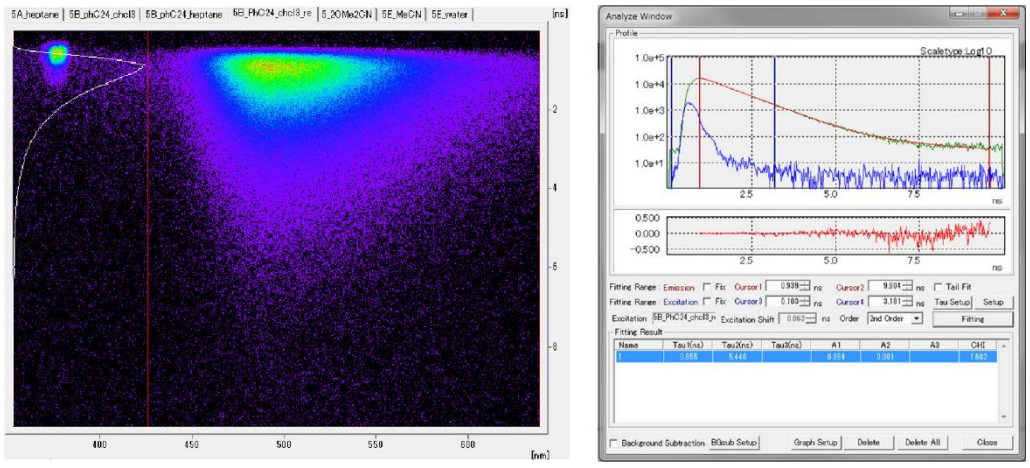

Figure S16. Streak image (left) and fluorescence decay analysis (right) of compound **3b** in $CHCl_3$ ($c = 1.0 \times 10^{-4}$ M).

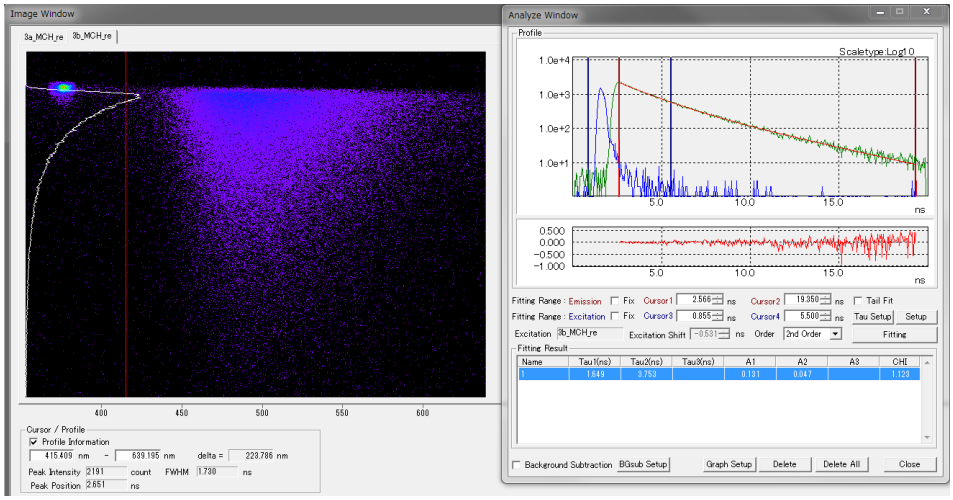

Figure S17. Streak image (left) and fluorescence decay analysis (right) of compound **3b** in MCH ($c = 1 \times 10^{-4}$ M).

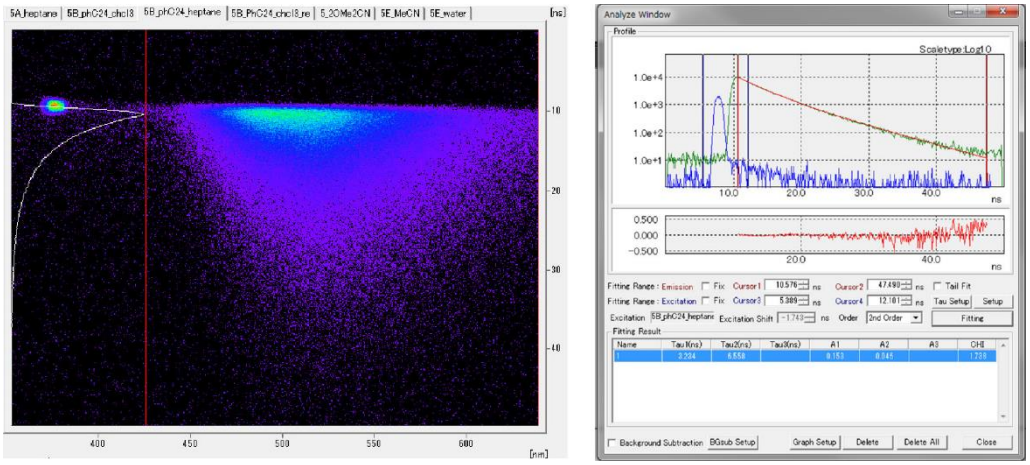

Figure S18. Streak image (left) and fluorescence decay analysis (right) of compound **3b** in heptane ($c = 1.0 \times 10^{-4}$ M).

Excited states of compounds 3a and 3b

Table S2. Excited states of 3a calculated at the TD-B3LYP/6-31g(d) level of theory

State[a]	Excitation energy		Oscillator strength	Major configurations (coefficeit)			
	/eV	/ nm					
$S_1@S_0$	3.0766	402.98	0.4483	HO	→	LU	(0.69688)
$S_2@S_0$	3.1189	397.52	0.0133	HO−2	→	LU	(0.60907)
$S_3@S_0$	3.1660	391.61	0.0083	HO−1	→	LU	(0.70291)
$S_1@S_1$	1.6944	731.75	0.1276	HO	→	LU	(0.70568)
$S_2@S_1$	2.4997	496.00	0.0118	HO	→	LU+1	(0.70290)
$S_3@S_1$	2.6823	462.23	0.2824	HO−1	→	LU	(0.70308)
$S_1@S_2$	2.2068	561.83	0.2042	HO	→	LU	(0.69372)
$S_2@S_2$	2.2519	550.59	0.0023	HO	→	LU+1	(−0.69346)
$S_3@S_2$	3.0044	412.67	0.0094	HO−2	→	LU	(−0.56028)

[a] $S_m@S_n$ denotes S_m state calculated using the optimized geometry of S_n.

Table S3. Excited states of 3b calculated at the TD-B3LYP/6-31g(d) level of theory

State[a]	Excitation energy		Oscillator strength	Major configurations (coefficeit)			
	/eV	/ nm					
$S_1@S_0$	2.9058	426.68	0.0204	HO−2	→	LU	(0.62738)
$S_2@S_0$	2.9343	422.54	0.4082	HO	→	LU	(0.70027)
$S_3@S_0$	3.0178	410.84	0.0100	HO−1	→	LU	(0.66139)
$S_1@S_1$	2.5223	491.55	0.0291	HO−1	→	LU	(0.60625)
				HO−2	→	LU	(0.32309)
$S_2@S_1$	2.6655	465.15	0.4747	HO	→	LU	(0.70238)
$S_3@S_1$	2.7602	449.18	0.0125	HO−2	→	LU	(0.61568)
				HO−1	→	LU	(−0.34001)
$S_1@S_2$	1.1953	1037.27	0.0366	HO	→	LU	(0.70481)
$S_2@S_2$	2.2326	555.35	0.0060	HO	→	LU+1	(−0.70459)
$S_3@S_2$	2.4638	503.22	0.2124	HO−1	→	LU	(−0.69327)

[a] $S_m@S_n$ denotes S_m state calculated using the optimized geometry of S_n.

Structural relaxation in the lowest energy excited state (S_1)

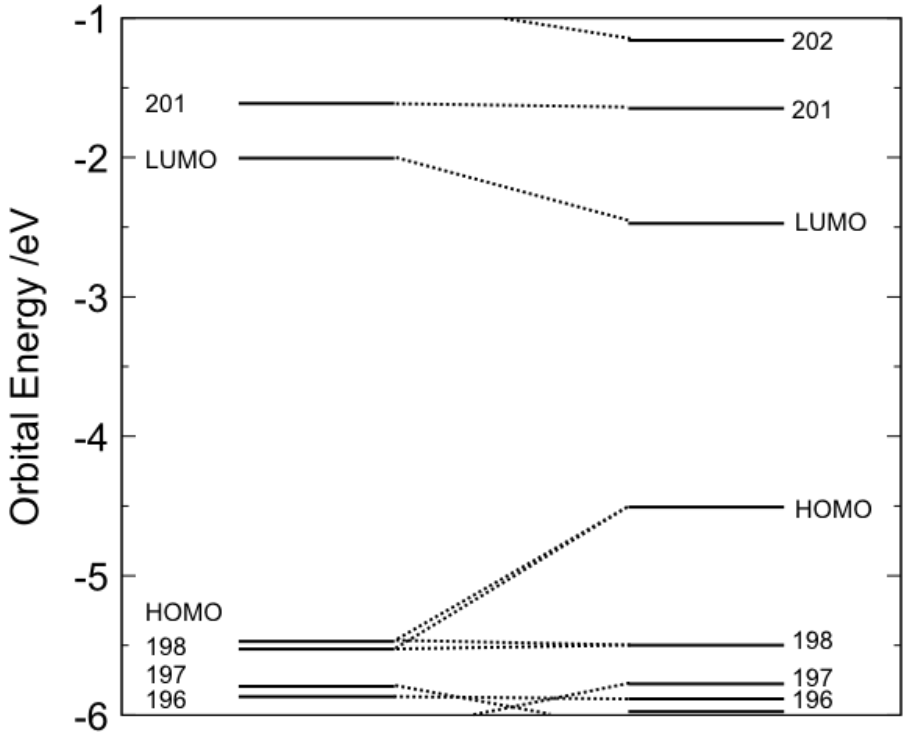

Figure S19. Level shifts of Kohn-sham frontier orbitals upon the vibrational relaxation of **3a** in the S_1 state (before, left; after, right)

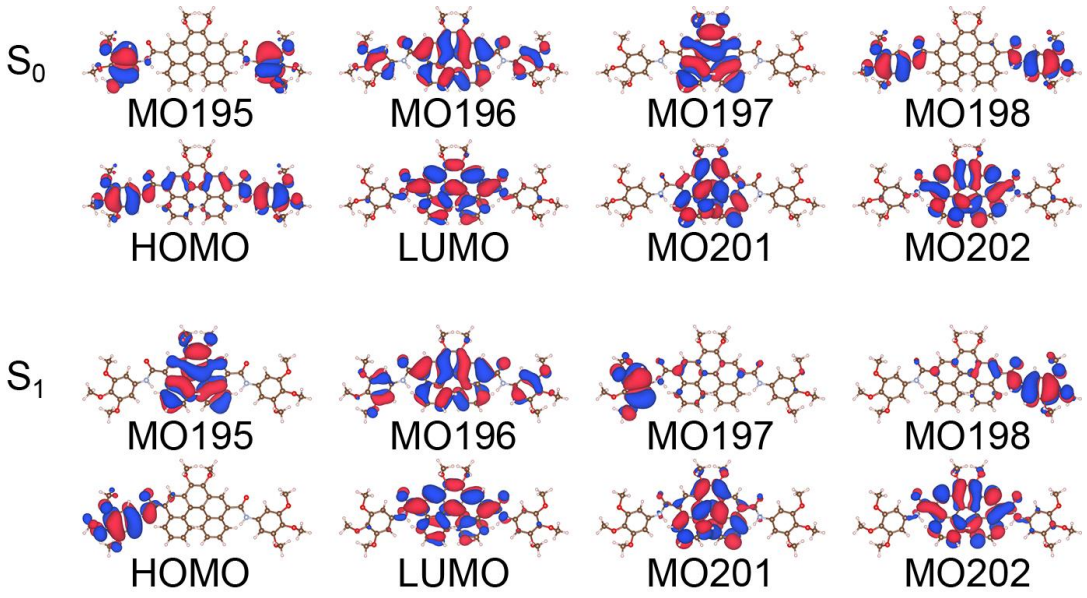

Figure S20. Kohn-Sham orbitals of **3a** in the ground (S_0) and excited (S_1) states.

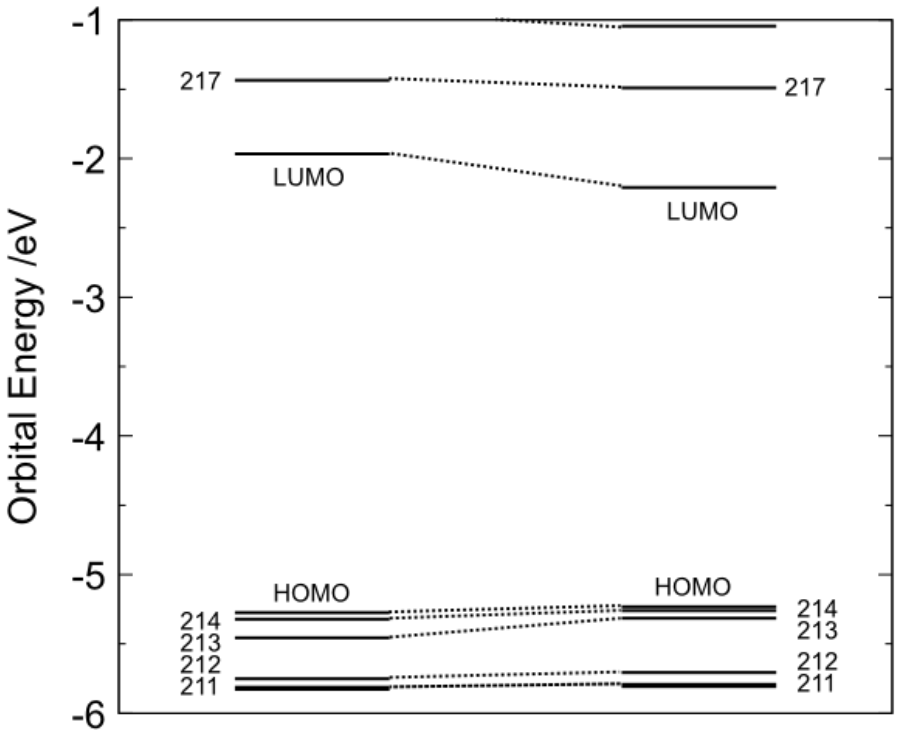

Figure S21. Level shifts of Kohn-sham frontier orbitals upon the vibrational relaxation of **3b** in the S_1 state (before, left; after, right)

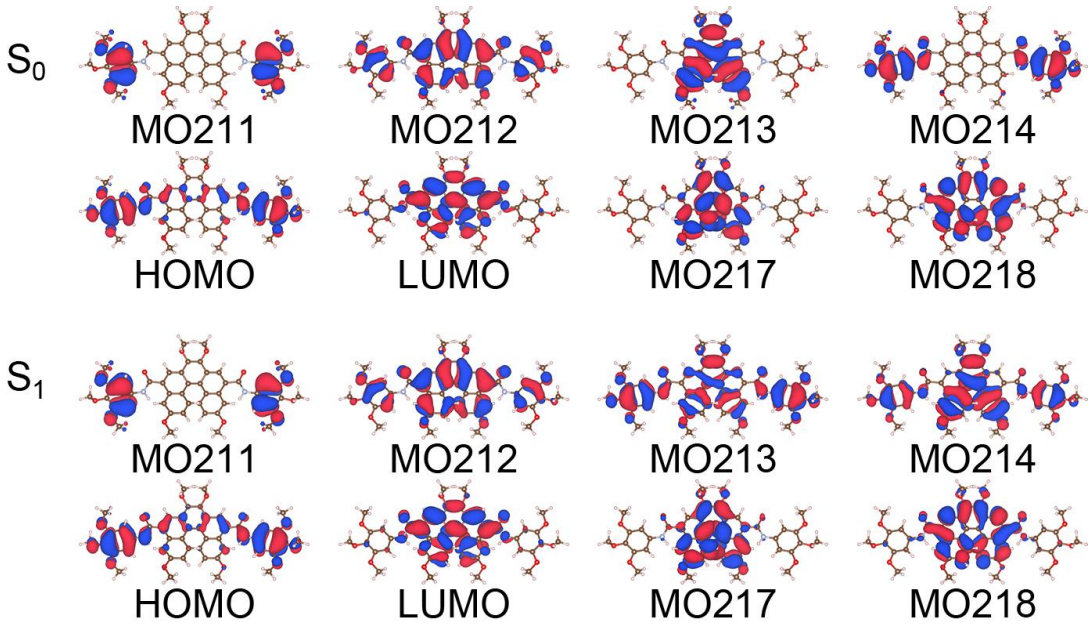

Figure S22. Kohn-Sham orbitals of **3b** in the ground (S_0) and excited (S_1) states.

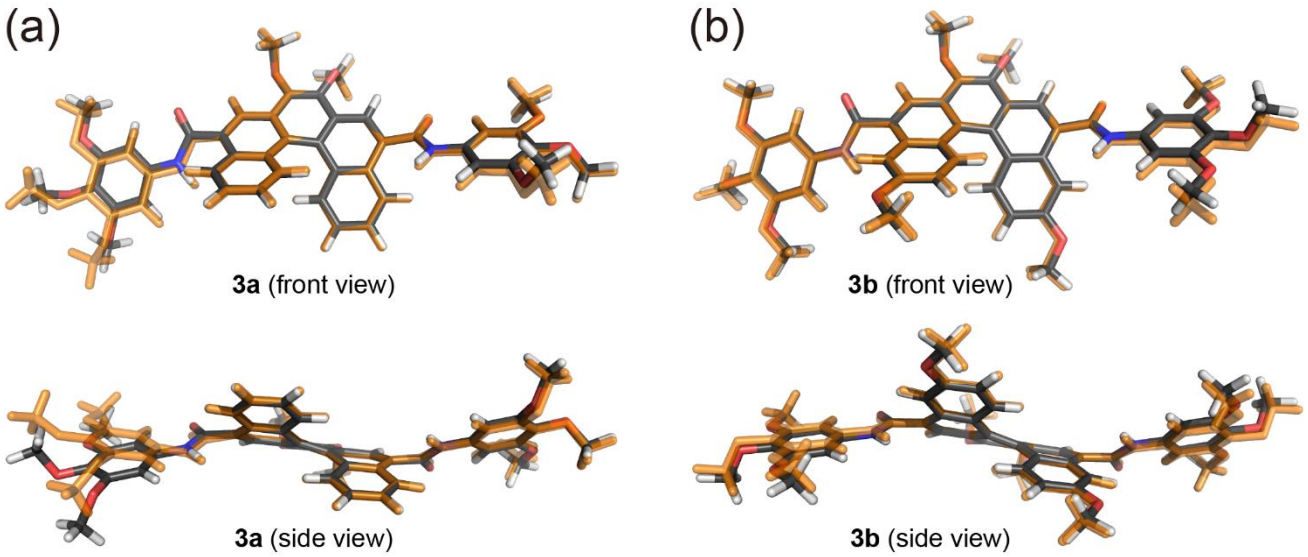

Figure S23. Superposition of optimized geometries of (a) **3a** and (b) **3b** in the ground state (S_0) and in the lowest energy excited state (S_1) calculated at the TD-B3LYP/6-31g(d) level of theory. The optimized structure in the S1 state is colored by orange. Because of the CT-type transition of compound **3a**, vibrational relaxation of **3a** (that is prominent in the left (3,4,5-trialkoxyphenyl)carbamoyl moiety) is larger than that of **3b**.

The result of diagonal vibronic coupling density (VCD) analysis

Table S4. Vibrational modes with large vibronic coupling (more than 1×10^{-4})

Compound	Mode#	Frequency / cm^{-1}	VCC / a.u.	Dim. Less VCC	Stabilization energy / eV
3a	191	1389.733	0.0002150914	0.4268768830	0.0156990306
	230	1577.764	0.0002797862	0.4590285531	0.0206090397
	232	1625.989	0.0003424703	0.5370602729	0.0290736723
3b	203	1387.674	0.0003829236	0.7616532026	0.0499043468
	253	1644.536	0.0002481866	0.3826394367	0.0149265383

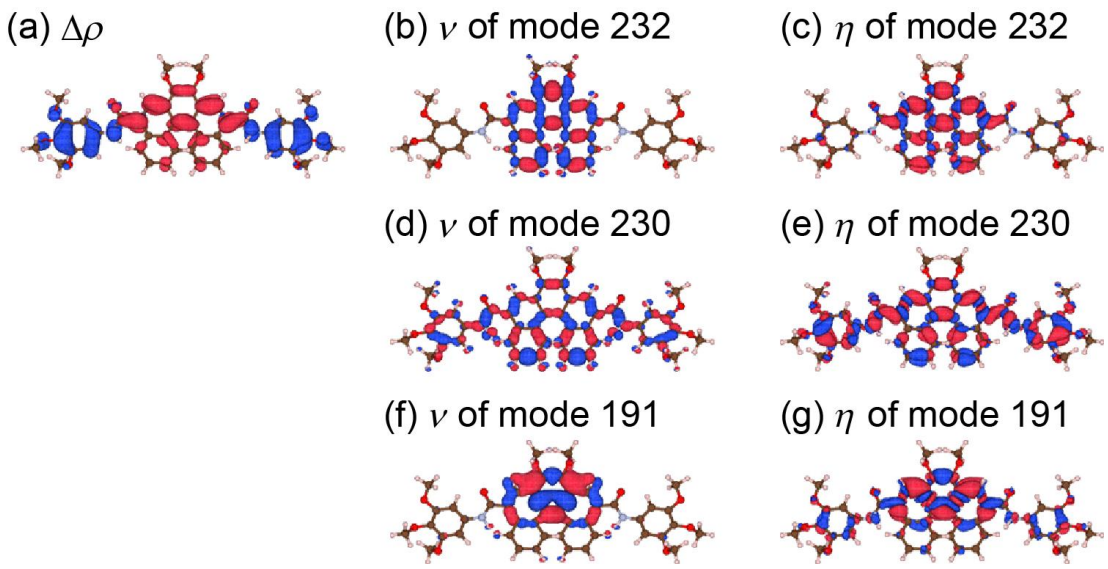

Figure S24. Diagonal vibronic coupling density (VCD) analysis for the S_1 Franck-Condon state of **3a**. (a) Electron density difference between S_1 and S_0 ($\Delta\rho$) (b,d,f) potential derivative (ν) of mode 232, 230, and 191, and (c,e,g) diagonal VCD (η) of mode 232, 230, and 191. The isosuface values are 0.01 a.u. for $\Delta\rho$, 0.003 a.u. for ν, and 1.0×10^{-6} a.u. for η.

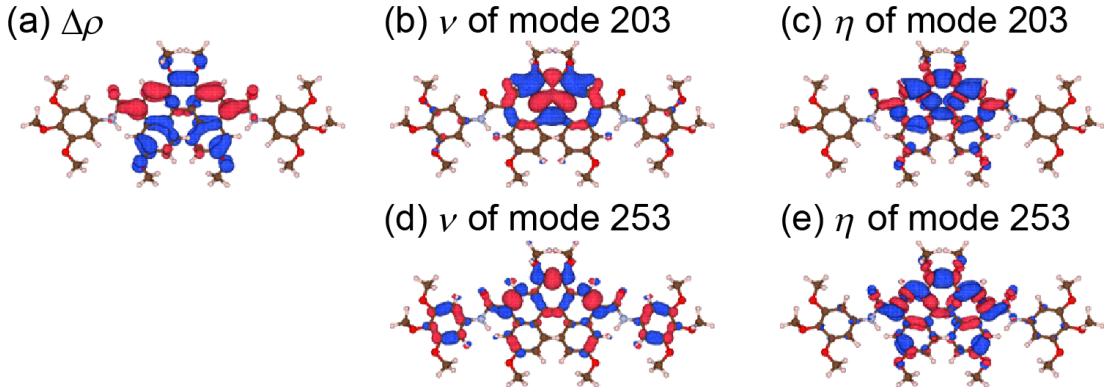

Figure S25. Diagonal vibronic coupling density (VCD) analysis for the S_1 Franck-Condon state of **3b**. (a) Electron density difference between S_1 and S_0 ($\Delta\rho$) (b,d) potential derivative (ν) of mode 203 and 253, (c,e) diagonal VCD (η) of mode 203 and 253. The isosuface values are 0.01 a.u. for $\Delta\rho$, 0.003 a.u. for ν, and 1.0×10^{-6} a.u. for η.

The result of off-diagonal vibronic coupling density (VCD) analysis

Off-diagonal vibronic coupling constant (VCC) of compound **3b** is larger than that of **3a**, which is associated with the local excitation (LE) property in the S_1 state of **3b**. When the S_0-S_1 transition is localized in a part of molecule, overlap density between S_1 and S_0 states (ρ_0) becomes large. A large ρ_0 gives rise to a large off-diagonal VCC, therefore, non-radiative decay constant (k_{nr}) tends to be large. The observed large off-diagonal VCC values for compound **3b** is consistent with the experimentally determined k_{nr} value in the monomer state (k_{nr} = 0.94 ns^{-1}).

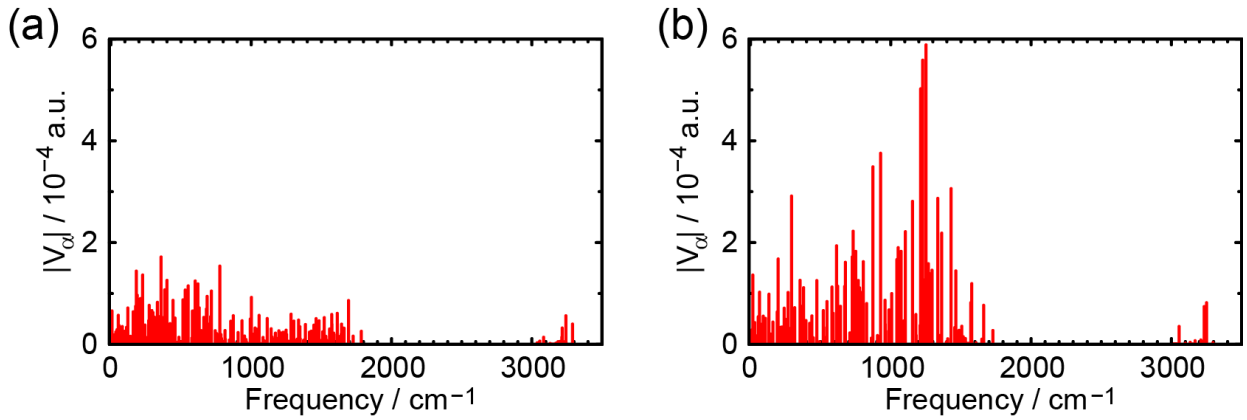

Figure S26. Off-diagonal vibronic coupling constant (VCC) for the nomal modes of (a) **3a** and (b) **3b**.

Table S5. Vibrational modes with large VCC between S_1 and S_0 states

Compound	Mode#	Frequency / cm^{-1}	VCC / 10^{-4} a.u.
3a	61	357.7601	1.7187015
	106	776.0229	1.5383858
	36	181.4421	1.4413278
3b	186	1251.112	5.8833112
	182	1227.696	5.5838244
	175	1212.957	5.0215513

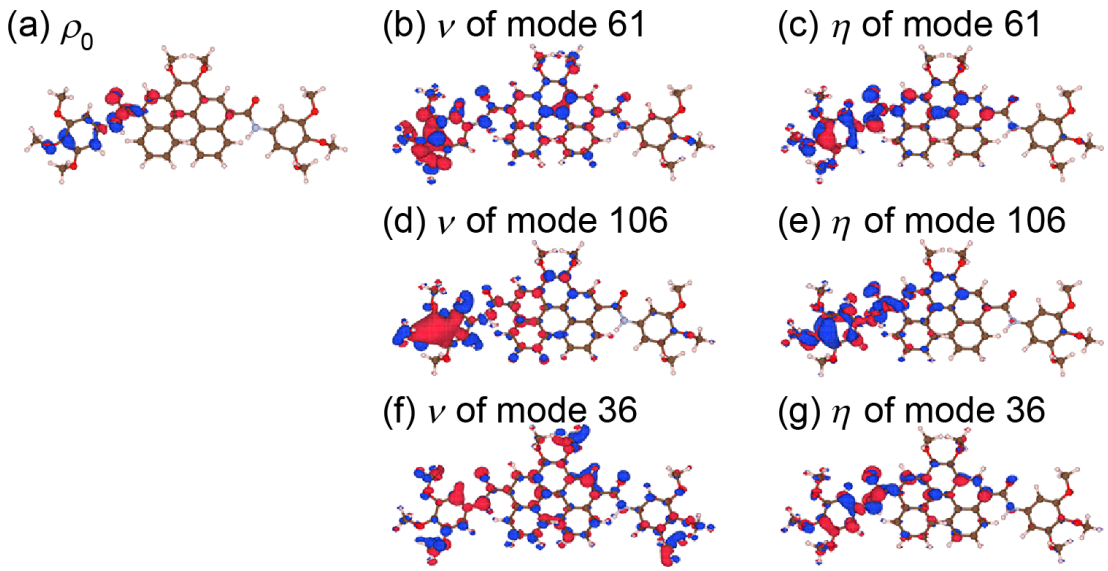

Figure S27. Off-diagonal vibronic coupling density (VCD) analysis for the S_1 adiabatic state and S_0 state of **3a**. (a) Overlap density between S_1 and S_0 (ρ_0), (b,d,f) potential derivative (ν) of modes 61, 106, and 253, (c,e,g) off-diagonal VCD (η) of modes 61, 106, and 36. The isosuface values are 0.01 a.u. for ρ_0, 0.003 a.u. for ν, and 1.0×10^{-6} a.u. for η.

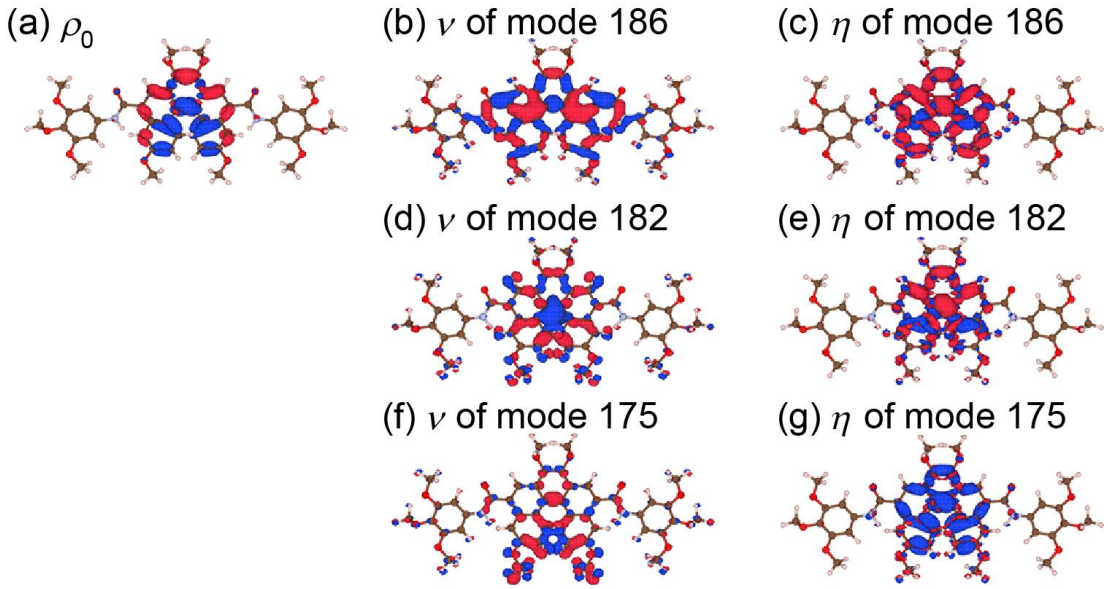

Figure S28. Off-diagonal vibronic coupling density (VCD) analysis for the S_1 adiabatic state and S_0 state of **3b**. (a) Overlap density between S_1 and S_0 (ρ_0), (b,d,f) potential derivative (ν) of modes 186, 182, and 175, (c,e,g) off-diagonal VCD (η) of modes 186, 182, and 175. The isosuface values are 0.01 a.u. for ρ_0, 0.003 a.u. for ν, and 1.0×10^{-6} a.u. for η.

Fragment molecular orbital (FMO) analysis

To elucidate the origin of the CT excitation in **3a**, we performed the fragment molecular orbital (FMO) analyses of **3a** and **3b**. The orbital interactions in **3a** and **3b** are depicted in Figs. S26.

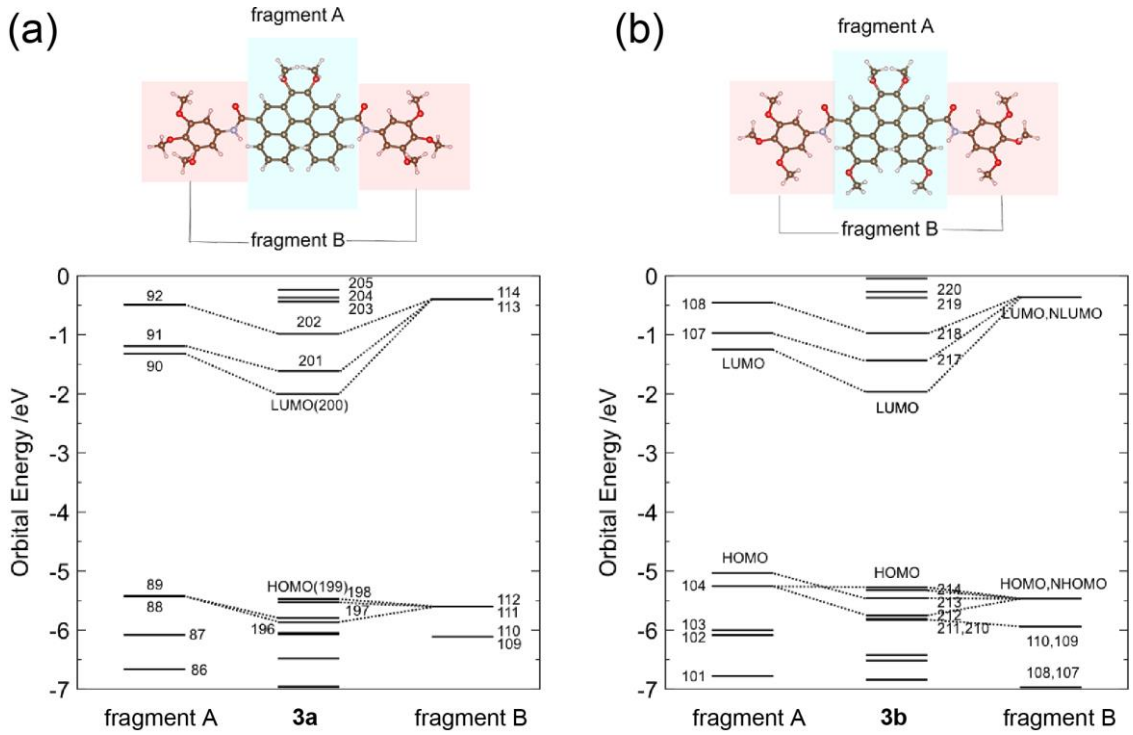

Figure S29. Orbital interactions in (a) compound **3a** and (b) **3b**. Left, orbital correlation diagram of fragment A; center, whole molecule; right, fragment B. The terminal of each fragment was replaced by hydrogen atom for the calculation of fragments. The fragments were calculated at B3LYP/6-31g(d) level of theory.

In the case of compound **3a**, the FMO levels of fragment A (i.e., MO89 and MO88) locate close to those of fragment B (i.e., MO112 and MO111) in **3a**. The resulting MOs of **3a**—that is localized in fragment A—are HOMO−2 and HOMO−3 (i.e., MO196 and MO197). Since the two fragments strongly interact, MO196 and MO197 are stabilized away from the frontier level (MO199). Accordingly, the frontier HOMO and HOMO−1 is of fragment B. On the other hand, the LUMO is greatly delocalized on fragment A.

The S_1 state of **3a** is a HOMO-LUMO excitation, while that of **3b** is a (HOMO−2)-LUMO excitation. The HOMO and HOMO−2 of **3b** (MO215 and MO213) are nearly degenerate. On the other hand, the HOMO and HOMO−2 in **3a** (MO199 and MO197) is separated, because of the strong orbital interaction in the HOMO−2 between the occupied frontier orbitals of fragments A and B. Therefore, the S_1 excitation of **3a** is the HOMO-LUMO excitation of the CT type from fragment B to fragment A.

As shown in Fig. S26, the levels of the HOMO and HOMO−1 of [5]helicene core (fragment A) in **3b** are separated because of the methoxy group. The HOMO level of fragment A is slightly higher than that of fragment B. As is the same in **3a**, the HOMO of fragment A in **3b** is stabilized because of the orbital interaction with the HOMO of fragment B. It should be noted that the resulting HOMO−2 of **3b** is close to the HOMO and HOMO−1 of **3b**, since the stabilization due to the orbital interaction between fragment A and fragment B compensates the level shift of the fragment A HOMO due to the methoxy substitution.

^{1}H and ^{13}C NMR spectra

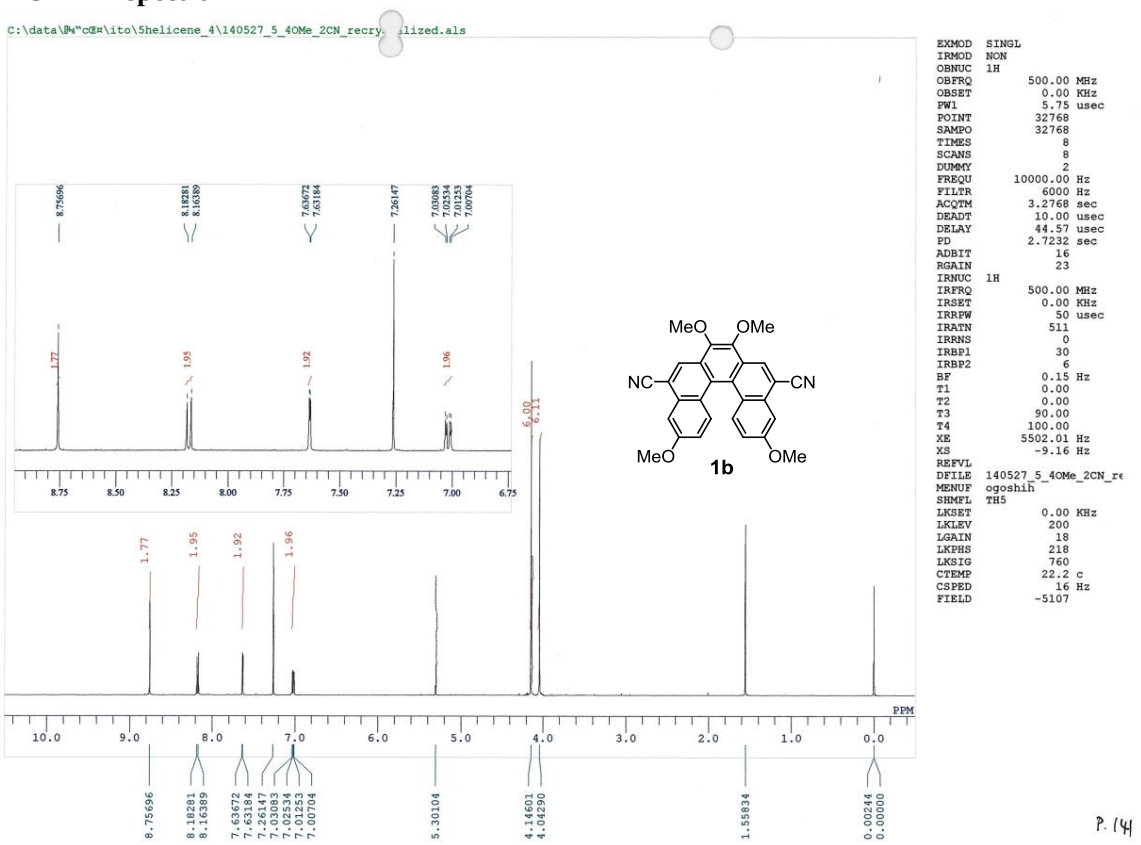

Figure S30. ^{1}H NMR spectra of compound **1b** ($CDCl_3$, 500 MHz)

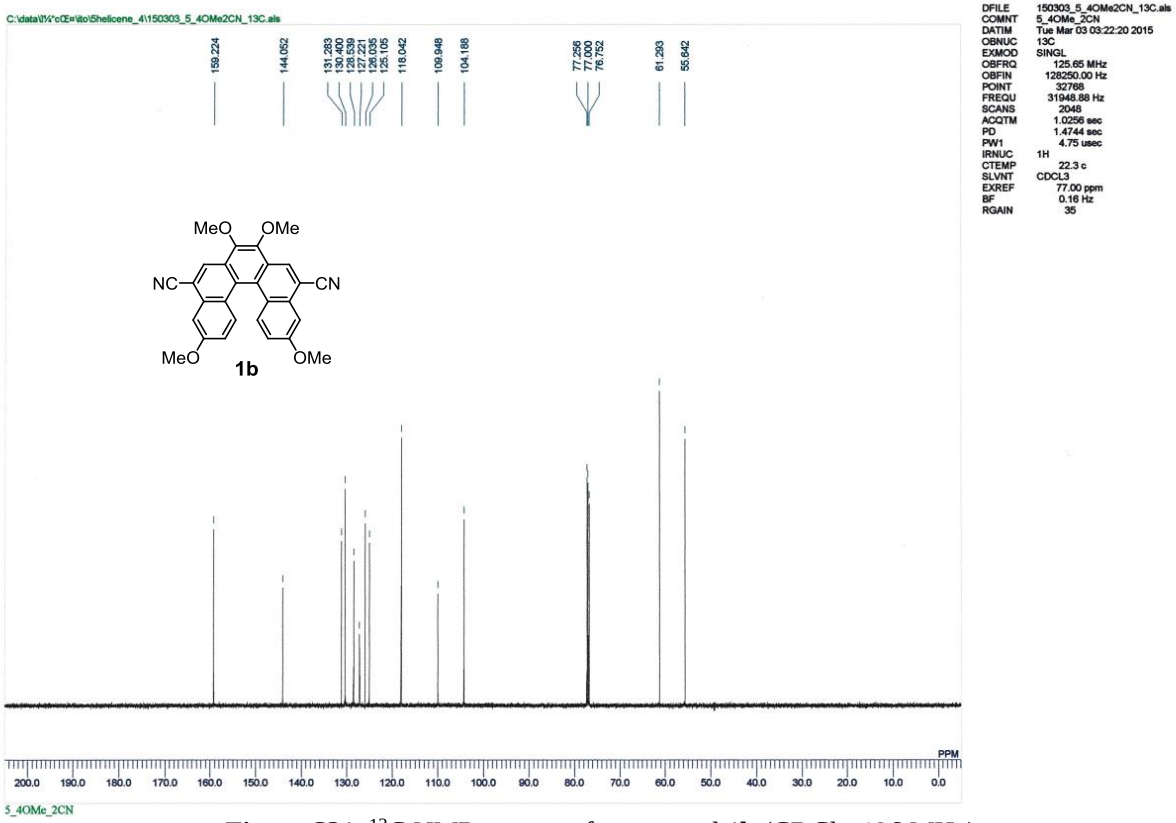

Figure S31. ^{13}C NMR spectra of compound **1b** ($CDCl_3$, 126 MHz)

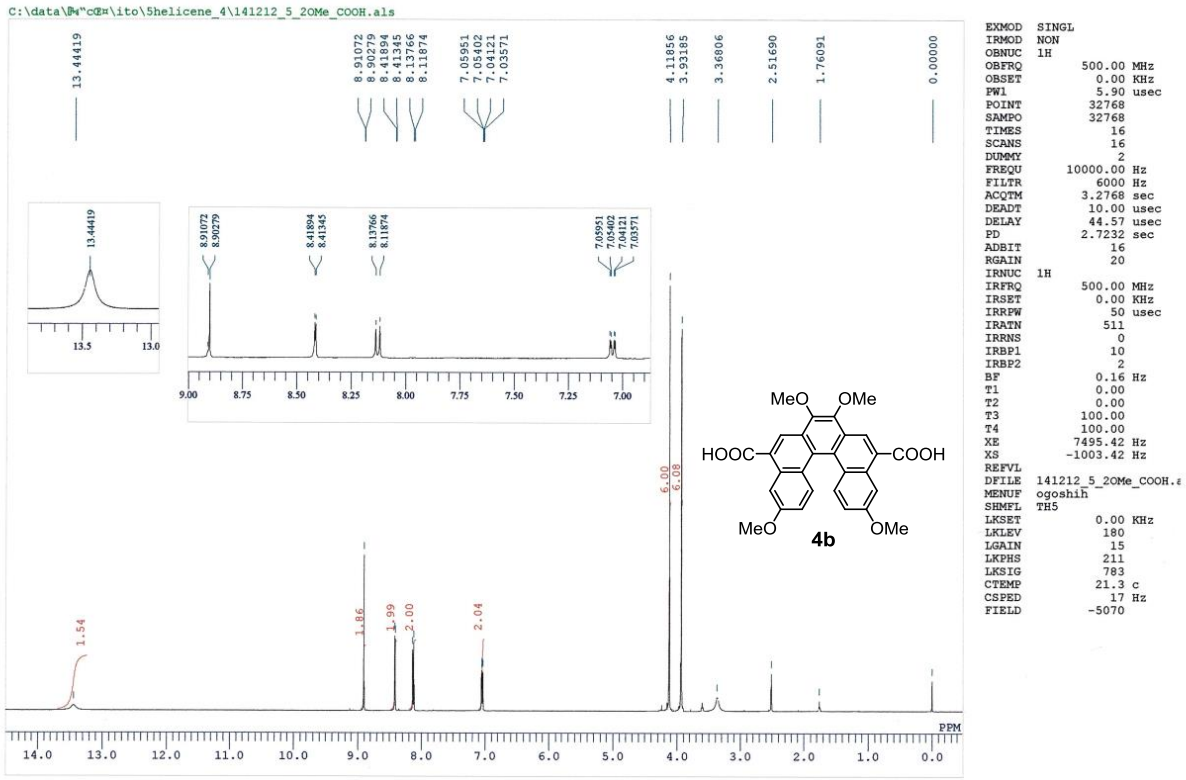

Figure S32. ^{1}H NMR spectra of compound **4b** (DMSO-d_6, 500 MHz)

5_2OMe_COOH

P. 41

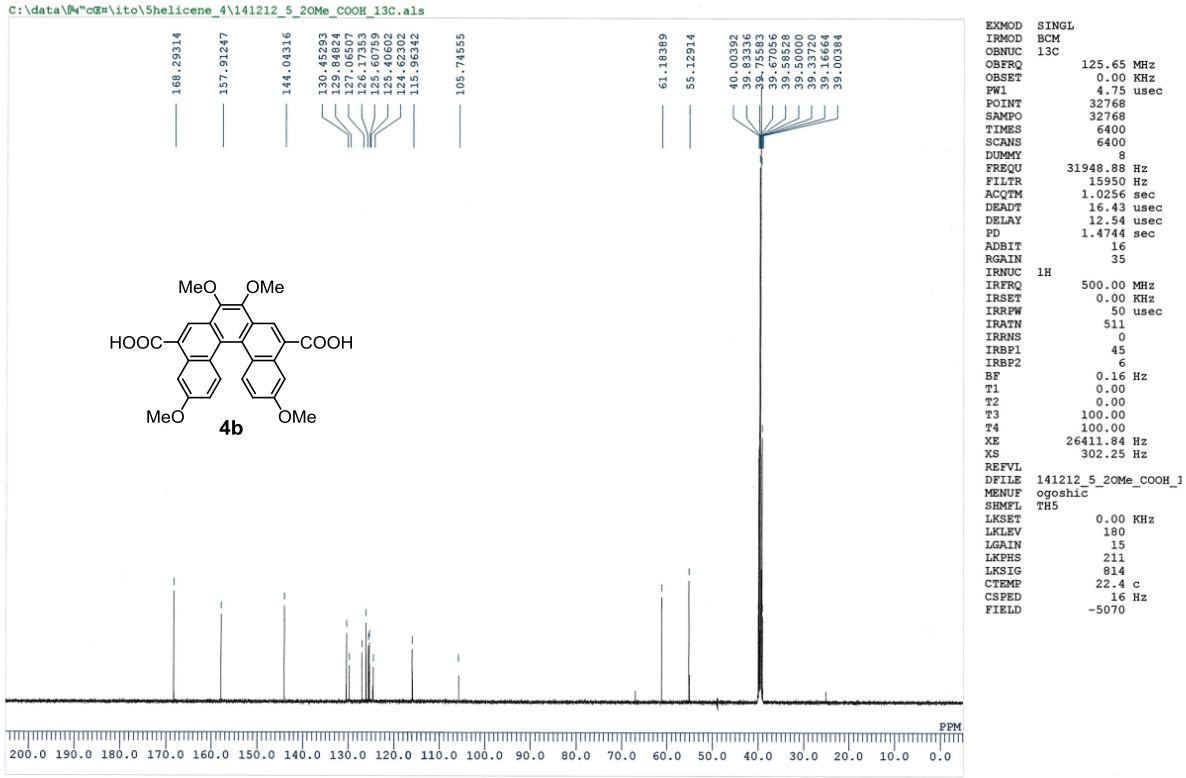

Figure S33. ^{13}C NMR spectra of compound **4b** (DMSO-d_6, 126 MHz)

5_2OMe_COOH

P-41

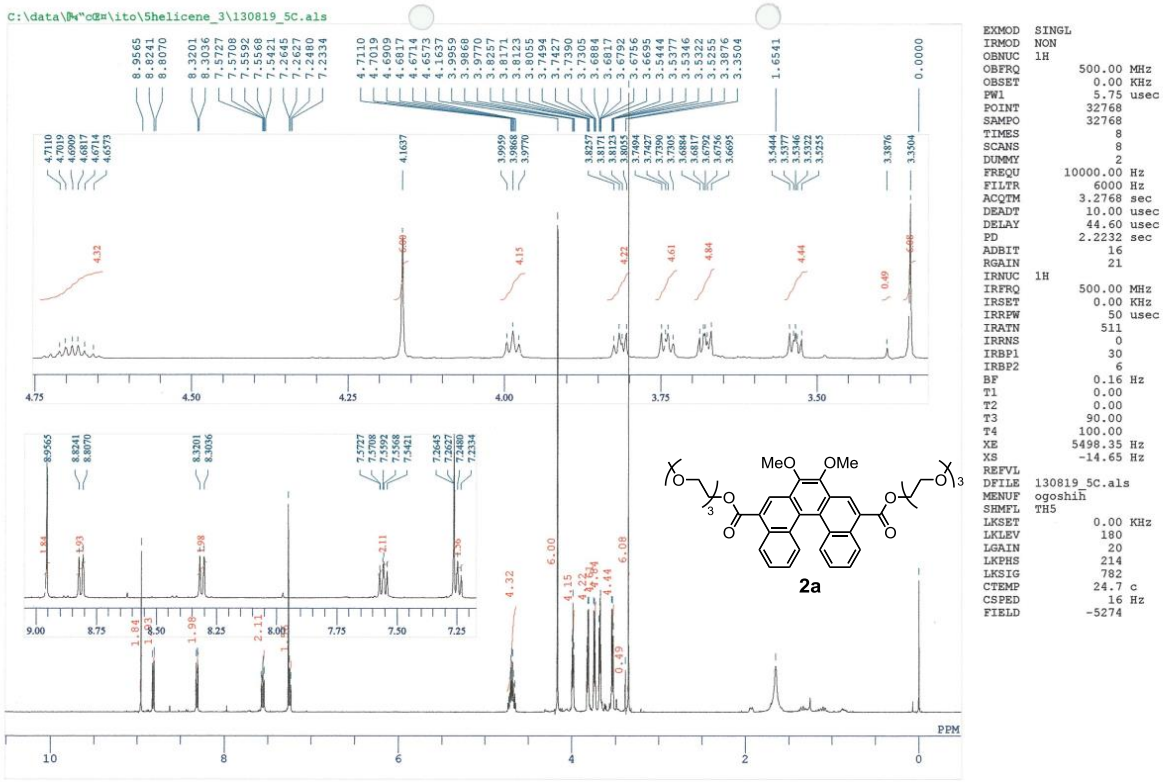

Figure S34. ^{1}H NMR spectra of compound **2a** ($CDCl_3$, 500 MHz)

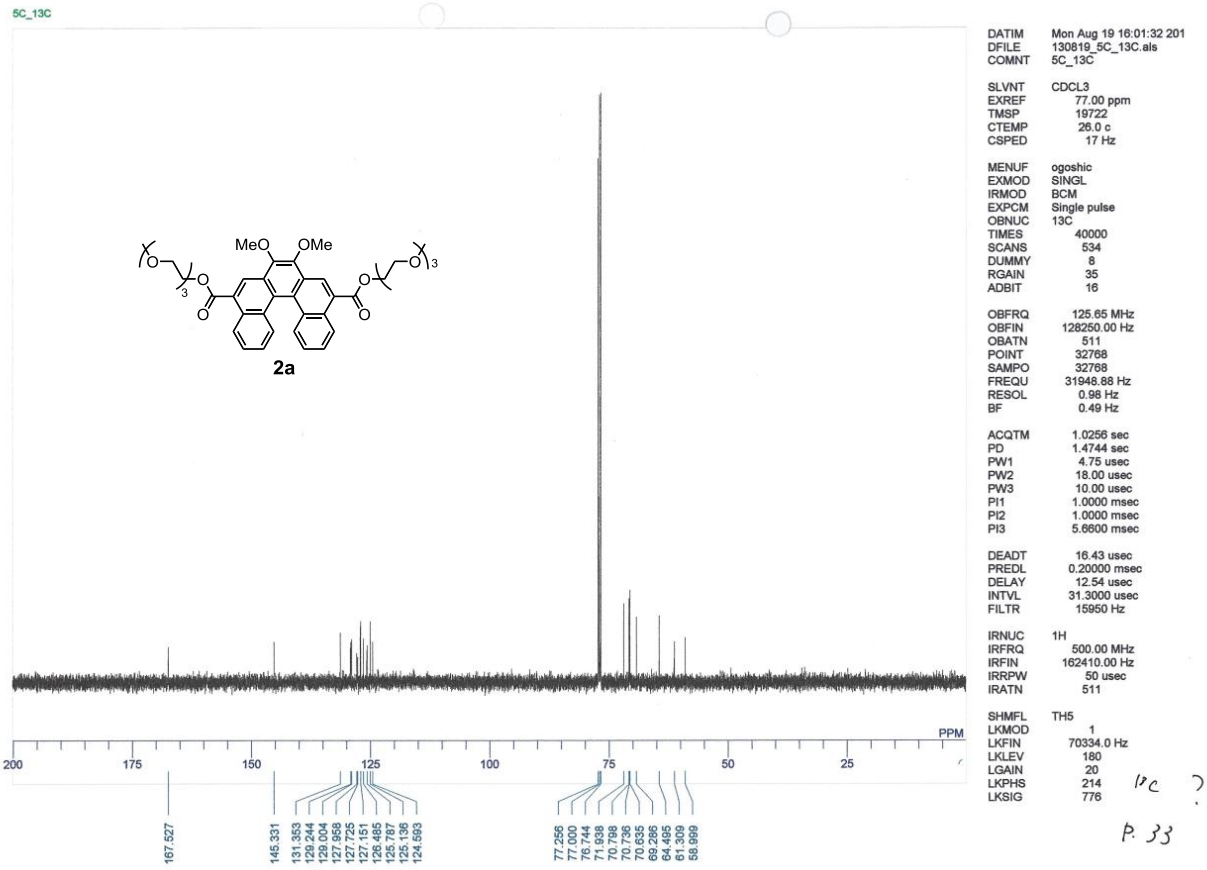

Figure S35. ^{13}C NMR spectra of compound **2a** ($CDCl_3$, 126 MHz)

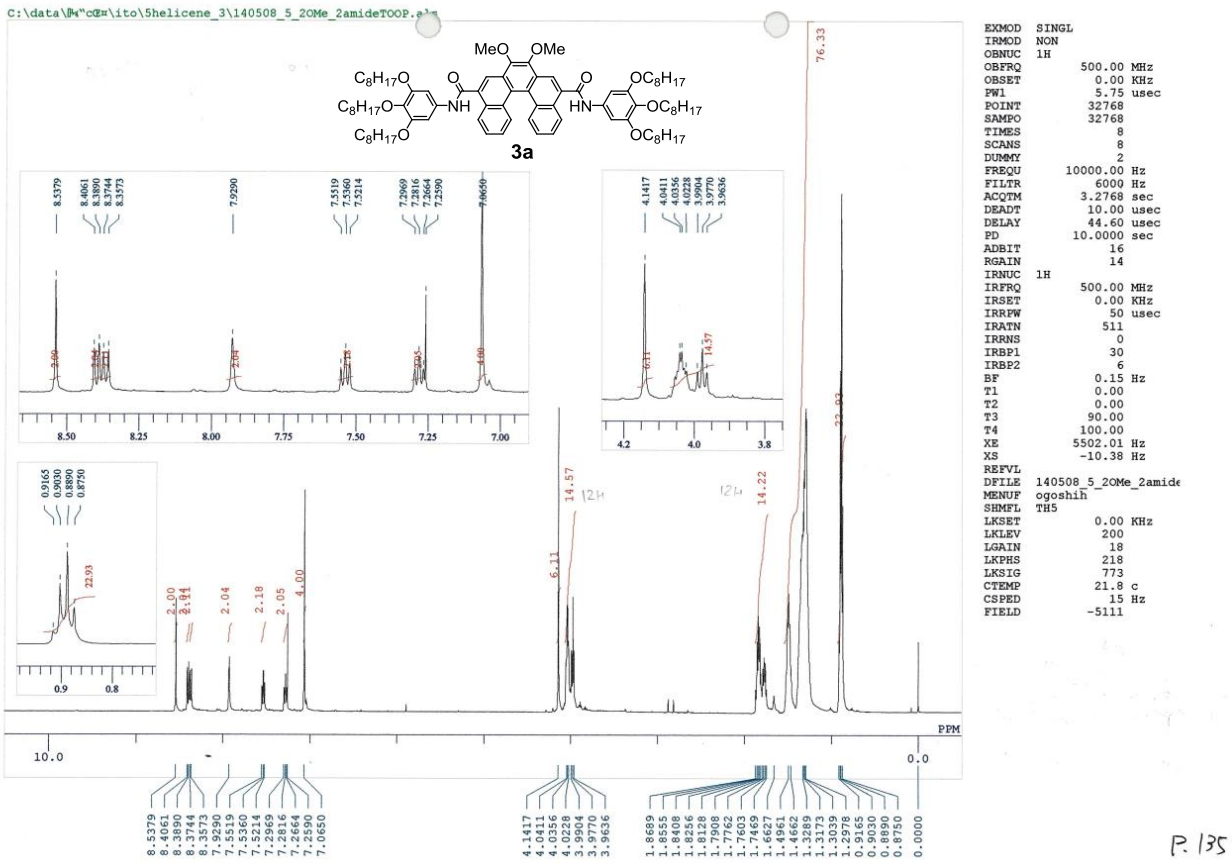

Figure S36. ^{1}H NMR spectra of compound **3a** ($CDCl_3$, 500 MHz)

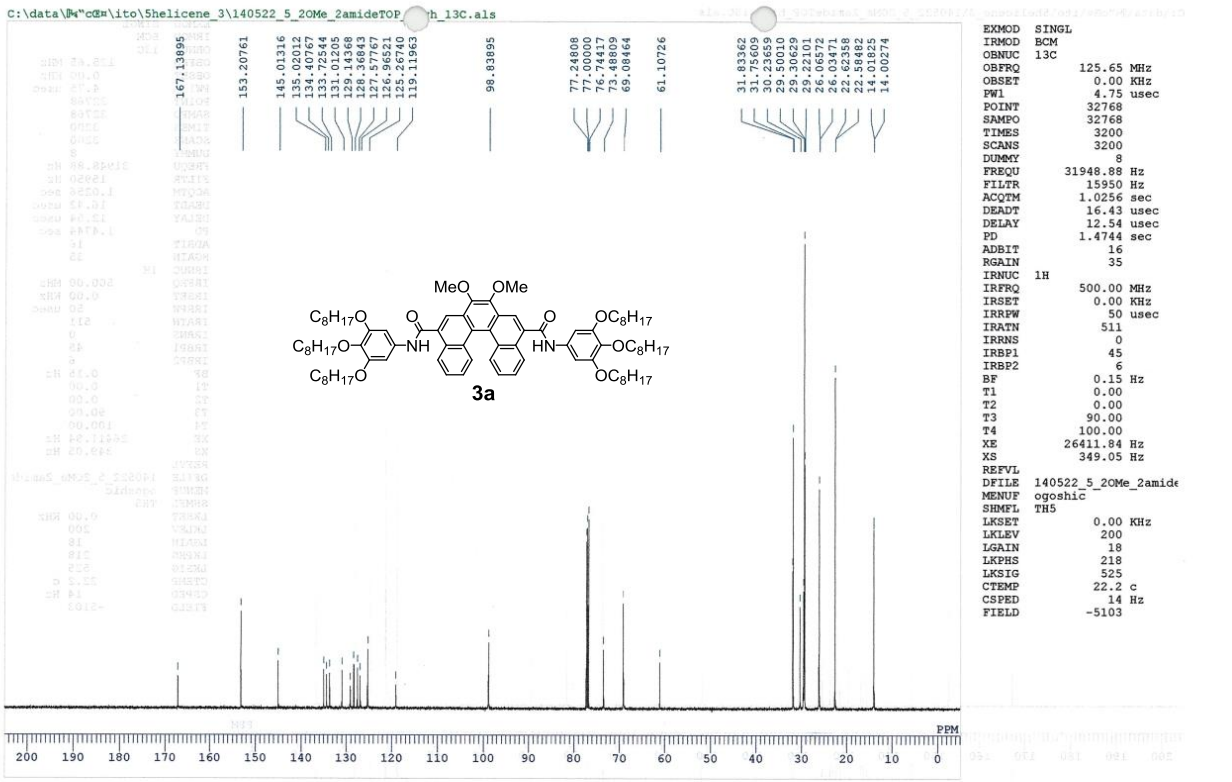

Figure S37. ^{13}C NMR spectra of compound **3a** ($CDCl_3$, 126 MHz)

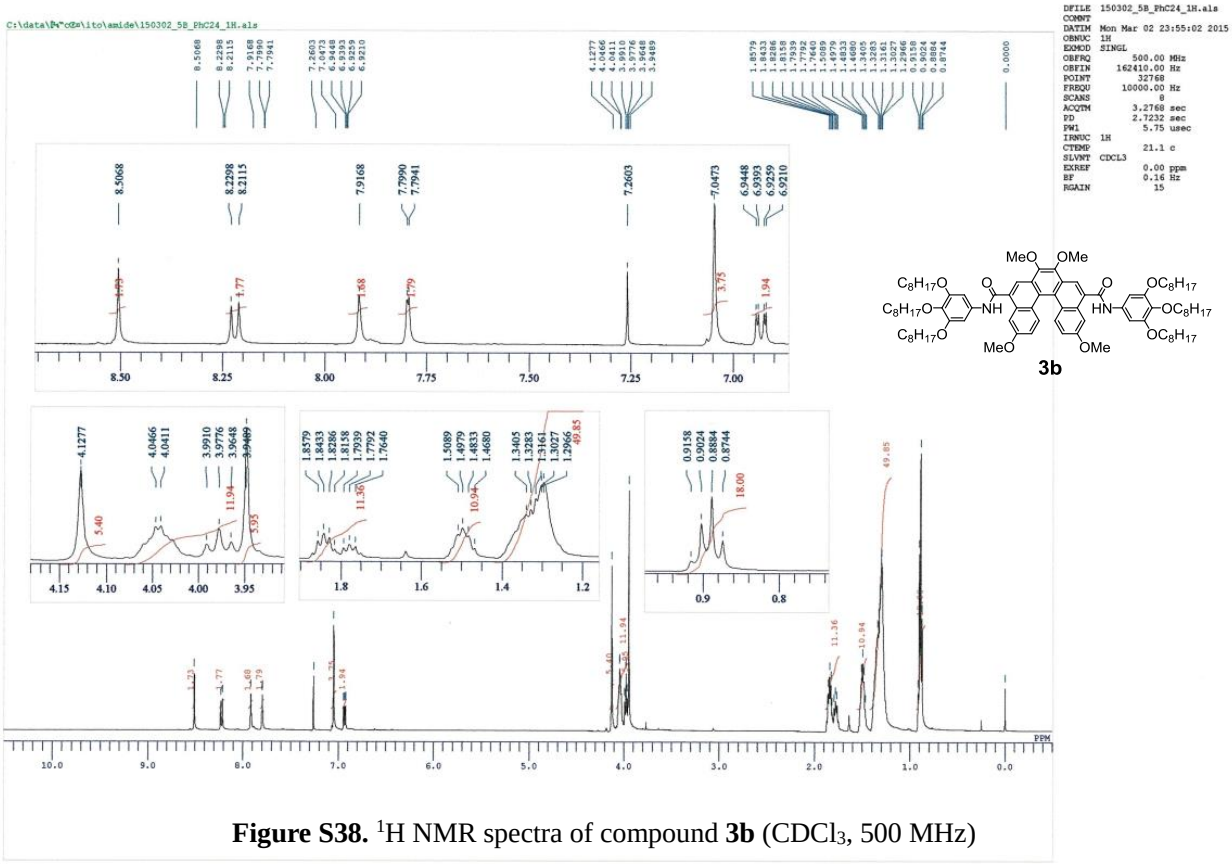

Figure S38. ^{1}H NMR spectra of compound **3b** ($CDCl_3$, 500 MHz)

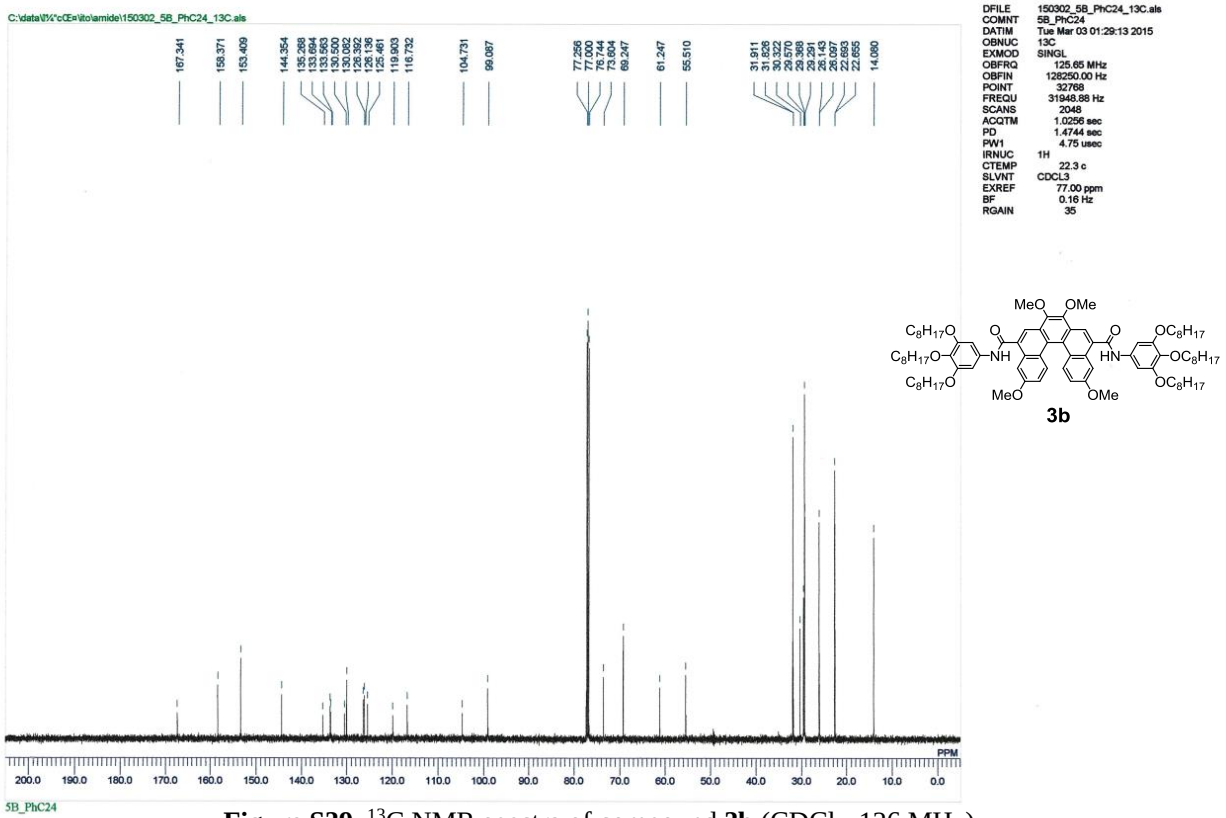

Figure S39. ^{13}C NMR spectra of compound **3b** ($CDCl_3$, 126 MHz)

References

(S1) Gaussian 09, Revision C.01, M. J. Frisch, G. W. Trucks, H. B. Schlegel, G. E. Scuseria, M. A. Robb, J. R. Cheeseman, G. Scalmani, V. Barone, B. Mennucci, G. A. Petersson, H. Nakatsuji, M. Caricato, X. Li, H. P. Hratchian, A. F. Izmaylov, J. Bloino, G. Zheng, J. L. Sonnenberg, M. Hada, M. Ehara, K. Toyota, R. Fukuda, J. Hasegawa, M. Ishida, T. Nakajima, Y. Honda, O. Kitao, H. Nakai, T. Vreven, J. A. Montgomery, Jr., J. E. Peralta, F. Ogliaro, M. Bearpark, J. J. Heyd, E. Brothers, K. N. Kudin, V. N. Staroverov, T. Keith, R. Kobayashi, J. Normand, K. Raghavachari, A. Rendell, J. C. Burant, S. S. Iyengar, J. Tomasi, M. Cossi, N. Rega, J. M. Millam, M. Klene, J. E. Knox, J. B. Cross, V. Bakken, C. Adamo, J. Jaramillo, R. Gomperts, R. E. Stratmann, O. Yazyev, A. J. Austin, R. Cammi, C. Pomelli, J. W. Ochterski, R. L. Martin, K. Morokuma, V. G. Zakrzewski, G. A. Voth, P. Salvador, J. J. Dannenberg, S. Dapprich, A. D. Daniels, O. Farkas, J. B. Foresman, J. V. Ortiz, J. Cioslowski, and D. J. Fox, Gaussian, Inc., Wallingford CT, 2010.

(S2) M. Uejima, T. Sato, D. Yokoyama, K. Tanaka, J.-W. Park, *Phys Chem. Chem. Phys.* 2014, **16**, 14244–14256.

(S3) M. Uejima, T. Sato, K. Tanaka, H. Kaji, *Chem. Phys.* 2014, **430**, 47–55.

(S4) Y. Nakai, T. Mori, Y. Inoue, *J. Phys. Chem. A*, 2012, **116**, 7372–7385.

(S5) For the relationship between the sign of [5]helicene derivatives and their absolute configurations, see: Y. Shen, H.-Y. Lu, C.-F. Chen, *Angew. Chem. Int. Ed.*, 2014, **53**, 4648–4651, and references therein.

(S6) R. H. Janke, T. Haufe, E.-U. Würthwein, J. H. Borkent, *J. Am. Chem. Soc.*, 1996, **118**, 6031–6035.